Black hole solutions surrounded by an anisotropic fluid in a Kalb–Ramond two-form background

Y. Sekhmani,[1,2,*] A. Al-Badawi,[3,†] Mohsen Fathi,[4,‡] A. Vachher,[5,§] and Sushant G. Ghosh[6,7,¶]

[1] *Center for Theoretical Physics, Khazar University, 41 Mehseti Street, Baku, AZ1096, Azerbaijan.*

[2] *Centre for Research Impact & Outcome, Chitkara University Institute of Engineering and Technology, Chitkara University, Rajpura, 140401, Punjab, India*

[3] *Department of Physics, Al-Hussein Bin Talal University 71111, Ma'an, Jordan*

[4] *Centro de Investigación en Ciencias del Espacio y Física Teórica (CICEF), Universidad Central de Chile, La Serena 1710164, Chile*

[5] *Centre for Theoretical Physics, Jamia Millia Islamia, New Delhi 110025, India*

[6] *Centre for Theoretical Physics, Jamia Millia Islamia, New Delhi - 110 025, India*

[7] *Astrophysics and Cosmology Research Unit, University of KwaZulu-Natal, Durban, South Africa*

(Dated: March 10, 2026)

We investigate static, spherically symmetric black hole spacetimes induced by the spontaneous Lorentz symmetry breaking of a Kalb–Ramond (KR) two-form field non-minimally coupled to gravity, coexisting with an anisotropic fluid. By adopting a general equation of state where the radial pressure relates to the energy density via $w_1 = -1$ and the tangential pressure via an arbitrary parameter w_2, we derive exact analytical solutions representing black holes surrounded by diverse matter fields, including dust ($w_2 = 0$), radiation ($w_2 = 1/3$), and dark energy-like distributions ($w_2 = -1/2$). A rigorous analysis of curvature invariants confirms a genuine core singularity, while the global geometry and adherence to standard energy conditions are shown to be highly sensitive to the interplay between the KR coupling (ℓ), the fluid density parameter (K), and w_2. Furthermore, we analyse null geodesics in detail to determine the photon sphere and shadow radii. Using the Gibbons-Werner geometrical approach and the Gauss-Bonnet theorem applied to the optical metric, we compute the weak deflection angle of light, demonstrating that both the KR field and the anisotropic fluid significantly enhance light bending, particularly in dark-energy-like backgrounds. Finally, we evaluate strong deflection limit (SDL) observables for the supermassive black holes Sgr A* and M87*, revealing quantifiable deviations from standard Schwarzschild geometries. These results offer novel astrophysical signatures for constraining string-inspired KR gravity and anisotropic dark matter halos using current and future observations.

arXiv:2603.07052v1 [gr-qc] 7 Mar 2026

I. INTRODUCTION

Lorentz invariance stands as the foundational cornerstone of modern theoretical physics, underpinning both the Standard Model of particle physics and General Relativity. While this symmetry has withstood rigorous experimental scrutiny across diverse energy scales, various high-energy frameworks including string theory and non-commutative field theories—postulate that it may falter at the Planck scale [1–8]. To systematically investigate these violations, the Standard Model Extension (SME) was established as a comprehensive effective field theory [9]. A prominent realisation of LSB within this framework is the Bumblebee model, in which a vector field (the "bumblebee" field) is non-minimally coupled to the gravitational sector. This field acquires a non-vanishing vacuum expectation value (VEV), triggering the symmetry breaking [10–13]. Notably, Casana et al. [14] derived a Schwarzschild-like black hole solution within this context, sparking extensive research into the astrophysical implications of bumblebee gravity [15–33]. Alternatively, LSB can be induced via a Kalb-Ramond (KR) field, i.e., a rank-two antisymmetric tensor field. Much like the bumblebee field, the KR field can couple non-minimally to gravity and develop a non-zero VEV [34]. The dynamics of KR-mediated symmetry breaking are detailed in [35–38], with a primary exact solution provided by [39]. Subsequent investigations have expanded on these foundations [40–42], including the derivation of alternative solutions that further probe the limits of Lorentz-violating spacetime [43].

A fundamental question in relativistic astrophysics concerns the nature of matter configurations that can maintain

* sekhmaniyassine@gmail.com
† ahmadbadawi@ahu.edu.jo (Corresponding author)
‡ mohsen.fathi@ucentral.cl
§ amnishvachher22@gmail.com
¶ sghosh2@jmi.ac.in

static equilibrium in the vicinity of a black hole. Although ordinary baryonic matter typically fails to achieve stability due to intense gravitational attraction and radiation pressure, certain field configurations, such as the electromagnetic stress-energy tensor in the Reissner-Nordström solution, demonstrate that equilibrium is possible when the pressure profile is inherently anisotropic [44, 45]. Specifically, these systems often feature a negative radial pressure ($p_r = -\rho$), suggesting that anisotropy and non-standard equations of state are essential for understanding the coexistence of compact objects and surrounding matter [46–48]. Traditionally, stellar and black hole models have relied on the Pascalian (isotropic) fluid approximation, a simplification supported by broad observational data in standard Einstein gravity [49–51]. However, as theoretical physics moves toward modified frameworks like massive gravity or KR theory, the role of local anisotropy has become a focal point of modern research [52–55]. Such anisotropy is not merely a mathematical curiosity; it arises naturally in self-gravitating systems with exotic thermodynamic properties or high-density regimes, such as quark stars or systems governed by barotropic equations of state [56–59]. Recent advancements, including the derivation of covariant Tolman-Oppenheimer-Volkoff (TOV) equations for non-isotropic fluids [60], have highlighted how pressure gradients significantly influence the structural stability and evolutionary trajectories of relativistic objects [55, 61]. Building upon this momentum, the present work explores a novel black hole solution within the context of KR gravity, specifically examining the gravitational and thermodynamic implications of an environmental anisotropic fluid coupled to the KR field's non-zero vacuum expectation value.

The investigation of gravitational lensing within the strong-field limit has emerged as a robust area of inquiry, primarily because relativistic images provide a unique window into the high-curvature environment immediately surrounding an event horizon. These images encode the subtle topological and geometric nuances of the spacetime, offering a powerful diagnostic for probing gravity where it is most extreme. While modified gravity theories often converge with General Relativity (GR) in the weak-field limit, the strong-field regime serves as a critical testing ground for identifying potential departures from Einsteinian physics. Consequently, gravitational lensing in this context is an indispensable tool for distinguishing between competing gravitational frameworks. The theoretical trajectory of this field began with Darwin's foundational study of light deflection around a Schwarzschild black hole [62]. This work laid the groundwork for Virbhadra and Ellis, who derived the definitive gravitational lens equation [63]. Subsequently, Bozza and collaborators [64] extended these analytical methods, enabling the systematic study of a diverse range of spacetimes beyond the standard Schwarzschild solution [65–68]. In the present study, we utilize these analytical formalisms to detect signatures of anisotropic fluid and Lorentz Symmetry Breaking (LSB). Building on existing literature regarding anisotropic signatures [69] and LSB effects in specific spacetimes [43, 70], we aim to quantify how these phenomena distort the path of electromagnetic radiation. To ensure our theoretical model remains physically grounded, we contrast our results with high-precision observational data. Specifically, we employ the deviation parameters δ established by observations of the Supermassive Black Holes (SMBHs) M87* [71, 72] and Sgr A* [73, 74]. By mapping our model's predictions against these empirical bounds, we can establish rigorous constraints on the theory's free parameters and assess its overall feasibility.

The structure of this paper is organized as follows: In Section II, we derive the static, spherically symmetric black hole solutions within the proposed framework. Section III is dedicated to the analysis of null geodesic trajectories, utilizing Event Horizon Telescope (EHT) data to establish rigorous constraints on the black hole parameters. Subsequently, Section IV investigates the weak deflection angle, while Sections V and VI provide a comprehensive study of strong gravitational lensing, further refining our parameter space in light of the M87* and Sgr A* observational bounds. Finally, Section VII summarizes our primary findings and outlines prospective avenues for future research regarding this black hole model.

II. BH SURROUNDED BY PFDM WITH A BACKGROUND KR FIELD

The Lorentz Symmetry Breaking (LSB) considered in this article is induced by a non-zero vacuum expectation value (VEV) of the KR two-form $B_{\mu\nu}$, an antisymmetric tensor of rank two. The KR sector is non-minimally coupled to gravity. Our objective is to obtain static, spherically symmetric black-hole solutions in which a background KR field coexists with an *anisotropic* matter distribution (henceforth the KR–anisotropic–fluid system). The total action we employ reads [34–40, 75–77]:

$$S = \int d^4x\sqrt{-g}\left[\frac{1}{2\kappa}\Big(R - 2\Lambda + \varepsilon\, B^{\mu\lambda}B^{\nu}{}_{\lambda}R_{\mu\nu}\Big) - \frac{1}{12}H_{\lambda\mu\nu}H^{\lambda\mu\nu} - V\big(B_{\alpha\beta}B^{\alpha\beta} \pm b^2\big) + \mathcal{L}_{\rm aniso}\right], \tag{1}$$

where $\kappa = 8\pi G$ (G being the Newtonian gravitational constant), ε is the non-minimal coupling constant, $b^2 > 0$ fixes the norm of the KR VEV, and Λ is the cosmological constant. The KR field strength is defined as $H_{\mu\nu\rho} \equiv \partial_{[\mu}B_{\nu\rho]}$. In

(1), $\mathcal{L}_{\rm aniso}$ denotes the Lagrangian density of the anisotropic fluid, which constitutes the primary matter sector. The self-interaction potential $V(X)$, where $X = B_{\alpha\beta}B^{\alpha\beta} \pm b^2$, triggers spontaneous Lorentz symmetry breaking, yielding a non-zero VEV $\langle B_{\mu\nu}\rangle = b_{\mu\nu}$ subject to the constraint $b_{\mu\nu}b^{\mu\nu} = \mp b^2$. In the vacuum configuration, this constraint implies that the KR field strength vanishes in the background.

Varying the action (1) with respect to $g^{\mu\nu}$ leads to the field equations:

$$R_{\mu\nu} - \frac{1}{2}g_{\mu\nu}R + \Lambda g_{\mu\nu} = \kappa\left(T^{\rm KR}_{\mu\nu} + T^{\rm M}_{\mu\nu}\right), \tag{2}$$

where $T^{\rm M}_{\mu\nu}$ is the energy-momentum tensor of the anisotropic fluid and $T^{\rm KR}_{\mu\nu}$ is the effective energy–momentum tensor of the KR field:

$$\begin{aligned}\kappa T^{\rm KR}_{\mu\nu} = {}& \frac{1}{2}H_{\mu\alpha\beta}H_{\nu}{}^{\alpha\beta} - \frac{1}{12}g_{\mu\nu}H^{\alpha\beta\rho}H_{\alpha\beta\rho} + 2V'(X)B_{\alpha\mu}B^{\alpha}{}_{\nu} - g_{\mu\nu}V(X)\\ &+\varepsilon\Big[\frac{1}{2}g_{\mu\nu}B^{\alpha\gamma}B^{\beta}{}_{\gamma}R_{\alpha\beta} - B^{\alpha}{}_{\mu}B^{\beta}{}_{\nu}R_{\alpha\beta} - B^{\alpha\beta}B_{\nu\beta}R_{\mu\alpha} - B^{\alpha\beta}B_{\mu\beta}R_{\nu\alpha}\\ &+\frac{1}{2}\nabla_\alpha\nabla_\mu\left(B^{\alpha\beta}B_{\nu\beta}\right) + \frac{1}{2}\nabla_\alpha\nabla_\nu\left(B^{\alpha\beta}B_{\mu\beta}\right) - \frac{1}{2}\nabla^\alpha\nabla_\alpha\left(B_\mu{}^\gamma B_{\nu\gamma}\right)\\ &-\frac{1}{2}g_{\mu\nu}\nabla_\alpha\nabla_\beta\left(B^{\alpha\gamma}B^{\beta}{}_{\gamma}\right)\Big].\end{aligned} \tag{3}$$

Here, the prime denotes the derivative with respect to the argument X. The Bianchi identities ensure the conservation of the combined tensor $T^{\rm KR}_{\mu\nu} + T^{\rm M}_{\mu\nu}$. In the subsequent analysis, we consider a vanishing cosmological constant ($\Lambda = 0$).

The anisotropic fluid contribution manifests through its energy-momentum tensor [78]:

$$T^{\rm M}_{\mu\nu} = (\rho + p_2)u_\mu u_\nu + (p_1 - p_2)x_\mu x_\nu + p_2 g_{\mu\nu}, \tag{4}$$

where ρ is the energy density measured by a comoving observer, u^μ is the timelike four-velocity, and x^μ is a spacelike unit vector orthogonal to u^μ and the angular directions. The resulting stress–energy tensor,

$$T^{\nu}_{\mu} = \mathrm{diag}\big(-\rho(r),\, p_1(r),\, p_2(r),\, p_2(r)\big), \tag{5}$$

together with a static, spherically symmetric geometry, provides a flexible framework for describing both the interiors of ultra-dense objects and nontrivial matter distributions exterior to a black hole. Allowing the radial (p_1) and tangential (p_2) pressures to differ is physically well-motivated; such anisotropy naturally arises from electromagnetic fields, scalar condensates, or tangential stresses in dark-matter halos, crucially modifying equilibrium and stability properties compared to the perfect-fluid case.

To close the system, we introduce equations of state that relate pressure to energy density. Rather than imposing a single, global barotropic index, we adopt the more general ansatz

$$p_1(r) = w_1(r)\,\rho(r), \qquad p_2(r) = w_2(r)\,\rho(r), \tag{6}$$

where w_1 and w_2 may be radial functions and need not coincide. This parametrisation simultaneously captures the standard cosmological limits and genuine anisotropic behaviours:

- **Dust:** $w_1 = w_2 = 0$.
- **Radiation:** $w_1 = w_2 = 1/3$.
- **Dark energy (cosmological–constant limit):** $w_1 = w_2 \simeq -1/2$.
- **Phantom:** $w_i < -1$.

In particular, cold dark matter or PFDM profiles are naturally represented by $w_1 \approx 0$ while w_2 may deviate slightly from zero to encode small tangential stresses; conversely, a dominant negative radial pressure ($w_1 < 0$) models locally repulsive dark–energy–type behaviour.

To derive static, spherically symmetric solutions, we employ the metric ansatz:

$$ds^2 = -F(r)dt^2 + G(r)dr^2 + r^2 d\theta^2 + r^2\sin^2\theta d\phi^2. \tag{7}$$

We consider a pseudoelectric KR gravity field configuration in which only the b_{01} and b_{10} components are non-zero. The constant norm condition yields:

$$b_{01} = -b_{10} = |b|\sqrt{\frac{G(r)F(r)}{2}}. \tag{8}$$

Assuming the KR gravity field remains frozen at its VEV, the field equations reduce to:

$$-\frac{rG'(r) + \big(G(r)-1\big)G(r)}{r^2G(r)^2} = \frac{\ell}{2\,r^2F(r)^2G(r)^2}\,\mathcal{E}_0 - 8\pi\,\rho(r), \tag{9}$$

$$\frac{rF'(r) + F(r)\big(1-G(r)\big)}{r^2F(r)G(r)} = \frac{\ell}{2\,r^2F(r)^2G(r)^2}\,\mathcal{E}_1 + 8\pi\,p_1(r), \tag{10}$$

$$\frac{\mathcal{M}}{4rF(r)^2G(r)^2} = -\frac{\ell}{4rF(r)^2G(r)^2}\,\mathcal{E}_2 + 8\pi\,p_2(r). \tag{11}$$

with

$$\mathcal{E}_0 := r^2G(r)\,F'(r)^2 + rF(r)\Big(rF'(r)G'(r) - 2G(r)\big(rF''(r)+F'(r)\big)\Big) + 2F(r)^2G(r), \tag{12}$$

$$\mathcal{E}_1 := r^2G(r)\,F'(r)^2 + r^2F(r)\Big(F'(r)G'(r) - 2G(r)F''(r)\Big) + 2F(r)^2\big(rG'(r)+G(r)\big), \tag{13}$$

$$\mathcal{E}_2 := rG(r)\,F'(r)^2 + F(r)\Big(rF'(r)G'(r) - 2G(r)\big(rF''(r)+F'(r)\big)\Big) + 2F(r)^2G'(r), \tag{14}$$

$$\mathcal{M} := -rG(r)\,F'(r)^2 + F(r)\Big(2G(r)\big(rF''(r)+F'(r)\big) - rF'(r)G'(r)\Big) - 2F(r)^2G'(r). \tag{15}$$

Assuming $w_1 = -1$, subtracting Eq. (9) from Eq. (10) yields

$$\frac{d}{dr}\ln\big[F(r)G(r)\big] = 0, \tag{16}$$

hence $F(r)G(r) = C$. Imposing the usual asymptotic normalization fixes $C = 1$, hence $G(r) = F(r)^{-1}$. Consequently, the line element reduces to

$$ds^2 = -F(r)dt^2 + F(r)^{-1}dr^2 + r^2(d\theta^2 + \sin^2\theta\,d\phi^2). \tag{17}$$

This means that there exists a hypersurface-orthogonal Killing vector in the spacetime. Thus, the spacetime is static in the region where $f > 0$, and $\rho = \rho(r)$ and $p_2 = p_2(r)$ hold by consistency. Equation (9) can be formally integrated to give

$$F(r) = \frac{1}{1-\ell} - \frac{2m(r)}{r}, \tag{18}$$

where the mass function $m(r)$ is defined by

$$m(r) = 4\pi\int^r r'^2\rho(r')dr'. \tag{19}$$

Here, the integration constant is absorbed into the definition of $m(r)$. If one requires the analyticity of the spacetime at the center, it requires $m(r) \simeq m_3r^3 + m_5r^5 + \cdots$ around $r = 0$, where m_3, m_5 are the constants, which restricts the form of $\rho(r)$. Putting Eq. (18) to Eq. (11), we obtain the expression of p_2 in terms of ρ as

$$p_2 = \frac{1}{2}(\ell-1)\left(r\rho'(r) + 2\rho(r)\right), \tag{20}$$

which can also be obtained from the conservation law $\nabla^\mu T_{\mu\nu} = 0$.

The purpose of this work is to find analytic solutions of Einstein's equations. In this work, we restrict our interests to the exactly solvable case with

$$w_1 = -1. \tag{21}$$

When ρ plays the role of an energy density, the energy conditions restrict the matter kinds to physically allowed ones. Among the conditions, the positivity of energy density appears to be crucial. In addition to it, all the energy conditions require $w_2 \geq -1$. Specifically, the dominant energy condition requires $w_2 \leq 1$ and the strong energy condition requires $w_2 \geq 0$. Therefore, when $0 \leq w_2 \leq 1$, all the energy conditions are satisfied. Once we assume $p_2 = w_2\rho$, Eq. (20) is solved to give $m(r)$ for $w_2 \neq 1/2$, the density and the radial pressure,

$$m(r) = M + \frac{K\, r^{1+\frac{2w_2}{\ell-1}}}{2(1-\ell)}, \qquad \rho(r) = -p_1(r) = \frac{K\,(1-2w_2-\ell) r^{\frac{2(1+w_2-\ell)}{\ell-1}}}{8\pi(1-\ell)^2}, \tag{22}$$

where M and K are constants. For the energy density to be non-negative, we require

$$r_0^{2w_2} \equiv (1-2w_2-\ell)K \geq 0, \tag{23}$$

where the positive parameter r_0 of length (mass) scale was introduced for convenience because the dimension of the parameter K is dependent on the value of w_2. The energy density and the pressure are singular at the origin or at infinity when $w_2 > -1$ and $w_2 < -1$, respectively.

To have a smooth $w_2 \to (1-\ell)/2$ limit, we introduce a new mass parameter

$$M' \equiv M + \frac{r_0^{1-\ell}}{2(1-2w_2-\ell)}. \tag{24}$$

Then, the solutions for $w_2 = (1-\ell)/2$ can be specified by taking the limit $w_2 \to (1-\ell)/2$ from Eq. (22), which gives

$$m(r) = M' + \frac{r_0}{2}\log\frac{r}{r+r_0}, \qquad \rho(r) = \frac{r_0^{1-\ell}}{8\pi(1-\ell)^2\, r^3}.$$

All the other physical formulae for $w_2 = 1/2$ in this work can be obtained in the same manner. Therefore, we will not discuss the $w_2 = 1/2$ case separately. The metric function in Eq. (18) becomes

$$F(r) = \frac{1}{1-\ell} - \frac{2M}{r} - \frac{K}{1-\ell}\, r^{\frac{2w_2}{\ell-1}}, \tag{25}$$

where M and K can be rewritten by using Eqs. (23) and (24). Because we are interested in solutions involving matter, we restrict our attention to the case with $r_0 \neq 0$. For $1/2 < w_2 \leq 1$, the spacetime structure must be very similar to that of the Reissner-Nordström geometry in coupling to a self-interacting KR field. For $1/2 < w_2 \leq 1$ the anisotropic-fluid term is sufficiently short-ranged that it produces only a localized correction to the metric; as a consequence the causal and horizon structure closely resembles that of a Reissner–Nordström black hole when the geometry is coupled to a self-interacting KR two-form. In the isotropic limit $w_1 = w_2 = -1$, the combinations $M/(1-\ell)$ and $3K/(1-\ell)$ play the roles of an effective mass parameter and an effective cosmological term within the KR framework — and, for those values of ℓ that make the exponent $2w_2/(\ell-1)$ produce an r^2 scaling, the $K/(1-\ell)$ contribution reduces to an (anti-)de Sitter cosmological constant while $M/(1-\ell)$ is the ADM mass.

In Fig. 1 we display the behaviour of the metric function $f(r)$ for $M = 1$ and representative values of the KR coupling ℓ and the anisotropy parameter K. Two correlated effects are visible. First, the overall amplitude of $f(r)$ is raised as ℓ approaches unity because of the global prefactor $1/(1-\ell)$, which shifts the baseline and therefore moves the radial locations of simple zeros (horizons) systematically outward. Second, the anisotropic-fluid term $-K\, r^{2w_2/(\ell-1)}$ changes its radial scaling depending on the equation-of-state parameter w_2: for $w_2 = 0$ (dust) it reduces to a constant offset that primarily translates the curve without altering asymptotic decay; for $w_2 = 1/3$ (radiation) it decays at large r, producing a Reissner–Nordström–like inner/outer-root profile; and for $w_2 < 0$ (dark-energy–like) it grows with r, generating a cosmological-type rise which can introduce an additional cosmological root. Hence, Fig. 1 compactly illustrates how the interplay between the ℓ-controlled amplitude and the sign of the exponent $2w_2/(\ell-1)$ determines both the number of horizons and their radial positions across the parameter sweep.

Now, let us analyze the curvature singularities. The scalar curvature reads

$$R = \frac{2(\ell+w_2-1)r_0^{2w_2} r^{\frac{2w_2}{\ell-1}} + 2(1-\ell)^2\ell}{(\ell-1)^3 r^2}, \tag{26}$$

is generically singular at the origin due to the r^{-2} term. At infinity, it decays only when $w_2/(\ell-1) < 1$; if $w_2/(\ell-1) > 1$, the curvature diverges as $r \to \infty$, indicating a non-asymptotically flat geometry. The squared Ricci tensor is given by

$$R_{ab}R^{ab} = \frac{2(1-\ell)^4\ell^2 + 4(\ell-1)^3\ell r_0^{2w_2} r^{\frac{2w_2}{\ell-1}} + 2\left((1-\ell)^2 + w_2^2\right) r_0^{4w_2} r^{\frac{4w_2}{\ell-1}}}{(\ell-1)^6 r^4}, \tag{27}$$

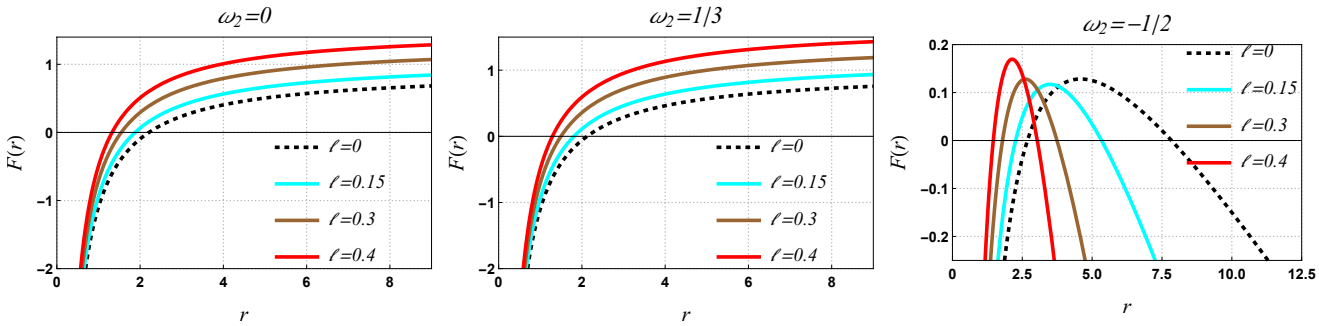

FIG. 1: $F(r)$ metric function with $K = 0.095$ and $M = 1$.

which diverges at the origin as r^{-4} (or more severely if $w_2/(\ell-1) < 0$). Similar to the Ricci scalar, it decays at infinity only for $w_2/(\ell-1) < 1$.

The Kretschmann invariant for this metric is given by

$$R_{abcd}R^{abcd} = \frac{4}{r^6}\left(\frac{4\left((\ell-1)^2M(\ell+2w_2-1) - w_2\, r_0^{2w_2}\, r^{\frac{2w_2}{\ell-1}+1}\right)^2}{(1-\ell)^4(\ell+2w_2-1)^2} + \left(2M + \frac{r}{\ell-1}\left(\frac{r_0^{2w_2}\, r^{\frac{2w_2}{\ell-1}}}{\ell+2w_2-1} + \ell\right)\right)^2 \right.$$
$$\left. + \frac{\left(2(\ell-1)^3M(\ell+2w_2-1) + w_2(-\ell+2w_2+1)\, r_0^{2w_2}\, r^{\frac{2w_2}{\ell-1}+1}\right)^2}{(1-\ell)^6(\ell+2w_2-1)^2}\right). \tag{28}$$

As $r \to 0$, the scalar generically diverges as r^{-6} (assuming $M \neq 0$), while its asymptotic behavior at large r is determined by the ratio $2w_2/(\ell-1)$. Specifically, the invariant decays for $2w_2/(\ell-1) < 2$ and approaches a non-zero limit or grows for $2w_2/(\ell-1) \geq 2$. On the other hand, the factors of $(\ell+2w_2-1)$ in the denominators appear to suggest a divergence, at $w_2 = (1-\ell)/2$; however, this is a coordinate-dependent artifact that is removable via the reparameterization (24), and thus does not constitute a physical curvature divergence. For $r_0 \neq 0$, the invariant remains regular everywhere only in the specific case $M = 0$ and $w_2 = -1$, which corresponds to (anti-)de Sitter space. In other parameter regimes, the curvature singularity, which is located at the origin or at infinity depending on the sign of $2w_2/(\ell-1)$, may be present, manifesting as either a black hole singularity hidden by horizons or a naked singularity, contingent upon the global horizon structure.

Energy conditions furnish indispensable criteria for assessing the physical admissibility of spacetime solutions and are routinely invoked in studies of both cosmological models [79] and black hole geometries [80, 81]. These conditions constrain the stress-energy tensor $T_{\mu\nu}$ in a manner that remains physically robust across Einstein gravity [82] and its various modifications [83]. The standard set—comprising the Null (NEC), Weak (WEC), Strong (SEC), and Dominant (DEC) energy conditions—is defined in terms of the energy density ρ and principal pressures P_i as follows:

$$\textbf{NEC}: \quad \rho + P_i \geq 0 \tag{29}$$
$$\textbf{WEC}: \quad \rho \geq 0, \qquad \rho + P_i \geq 0 \tag{30}$$
$$\textbf{SEC}: \quad \rho + \sum_i P_i \geq 0, \quad \rho + P_i \geq 0 \tag{31}$$
$$\textbf{DEC}: \quad \rho \geq 0, \qquad \rho \geq |P_i| \tag{32}$$

Relevant quantities are deduced as

$$\rho + p_1 = 0,\ \rho + p_{2,3} = \frac{K(w_2+1)(1-2w_2-\ell)r^{\frac{2w_2}{\ell-1}-2}}{8\pi(1-\ell)^2}, \tag{33}$$

$$\rho + p_1 + p_2 + p_3 = \frac{w_2K(1-2w_2-\ell)r^{\frac{2(w_2-\ell+1)}{\ell-1}}}{4\pi(1-\ell)^2}, \tag{34}$$

$$\rho - |p_1| = 0,\ \rho - |p_{2,3}| = \rho - \left|\frac{w_2\, K(1-2w_2-\ell)r^{\frac{2(w_2-\ell+1)}{\ell-1}}}{8\pi(1-\ell)^2}\right|. \tag{35}$$

- The Null Energy Condition (NEC) is saturated, $\rho + p_1 = 0$, while the tangential null combination is given by

$$\rho + p_{2,3} = \frac{(1+w_2)\,K(1-2w_2-\ell)\,r^{\frac{2w_2}{\ell-1}-2}}{8\pi(1-\ell)^2}.$$

  Therefore, the NEC is algebraically equivalent to

$$(1+w_2)\,K(1-2w_2-\ell) \geq 0.$$

  In particular:

  - $w_2 = -1$ saturates the tangential NEC.
  - For $w_2 > -1$ the NEC reduces to $K(1-2w_2-\ell) \geq 0$.
  - For $w_2 < -1$ the NEC requires $K(1-2w_2-\ell) \leq 0$.

- Using the displayed expression

$$\rho + \sum_i p_i = \frac{w_2\,K(1-2w_2-\ell)\,r^{\frac{2(w_2-\ell+1)}{\ell-1}}}{4\pi(1-\ell)^2},$$

  the SEC (both $\rho + \sum_i p_i \geq 0$ and $\rho + p_i \geq 0$) is equivalent to the pair of algebraic inequalities

$$w_2\,K(1-2w_2-\ell) \geq 0 \quad \text{and} \quad (1+w_2)\,K(1-2w_2-\ell) \geq 0. \tag{36}$$

  Consequences by w_2-region:

  - If $w_2 > 0$ then $w_2 > 0$ and $1 + w_2 > 0$, so the SEC reduces to $K(1-2w_2-\ell) \geq 0$.
  - If $-1 < w_2 < 0$ then $w_2 < 0$ while $1+w_2 > 0$; the two inequalities are incompatible unless $K(1-2w_2-\ell) = 0$. Hence, the SEC is generically violated for $-1 < w_2 < 0$.
  - If $w_2 < -1$ both w_2 and $1 + w_2$ are negative and the SEC can hold for $K(1-2w_2-\ell) \leq 0$.

- The radial DEC is saturated because $p_1 = -\rho$ gives $\rho - |p_1| = 0$. The tangential DEC condition is

$$\rho - |p_{2,3}| = \rho - \left| \frac{w_2\,K(1-2w_2-\ell)\,r^{\frac{2(w_2-\ell+1)}{\ell-1}}}{8\pi(1-\ell)^2} \right| \geq 0. \tag{37}$$

  For the solution family where ρ and $p_{2,3}$ share the same overall parameter factor S and the same radial scaling, the DEC reduces to the simple algebraic requirements

$$K(1-2w_2-\ell) \geq 0 \qquad \text{and} \qquad |w_2| \leq 1. \tag{38}$$

  Thus the DEC requires $K(1-2w_2-\ell) \geq 0$ together with $-1 \leq w_2 \leq 1$. (If the radial exponents differed, the condition would become radius-dependent and could hold only inside a restricted radial domain.)

Figure 2 shows radial profiles of ρ, $\rho + p_{2,3}$ and $\rho + \sum_i p_i$ for $K = 0.095$, $M = 1$ and varying ℓ with $w_2 = 0$. Hence, the tangential NEC is algebraically equivalent to

$$K(1-\ell) \geq 0, \tag{39}$$

the SEC is saturated ($\rho + \sum_i p_i = 0$), and the DEC reduces to $K(1-\ell) \geq 0$ together with $|w_2| \leq 1$ (here $|w_2| = 0$). The observed decrease in the amplitude of $\rho + p_{2,3}$ as ℓ approaches unity follows directly from $K(1-\ell)$: larger ℓ reduces $K(1-\ell)$ and pushes the tangential combination toward zero. The radial scaling for $w_2 = 0$ is r^{-2}, so the steep rise of the plotted combinations near the left axis corresponds to the core divergence implied by this exponent.

Figure 3 presents the parameter-dependent behavior of $K = 0.095$ with two representative equations of state: $w_2 = -1/2$ (left panel) and $w_2 = 1/3$ (right panel), using $\ell = 0.1$ in treatment. The controlling factor is evaluated to

$$K(2-\ell)\,\big|_{w_2=-\frac{1}{2}} > 0, \qquad K\left(\tfrac{1}{3}-\ell\right)\big|_{w_2=\frac{1}{3}} > 0 \ (\text{for } \ell = 10^{-1}). \tag{40}$$

The energy-condition pattern follows from the algebraic sign rules:

- For $w_2 = -1/2$: $1+w_2 = +1/2 > 0$ and $K(2-\ell) > 0$, so the tangential NEC $(1+w_2)K(2-\ell)$ is positive; $|w_2| < 1$ and $K(2-\ell) > 0$ imply that DEC holds pointwise; however, $w_2 < 0$ with $K(2-\ell) > 0$ yields $w_2 K(2-\ell) < 0$ and therefore $\rho + \sum_i p_i < 0$, i.e., SEC violation across the plotted radii. The radial slopes are mild, consistent with the less singular exponents for this choice of w_2.
- For $w_2 = 1/3$: $w_2 > 0$ and $1 + w_2 > 0$, so NEC, SEC and DEC reduce to the single algebraic requirement $K\left(\frac{1}{3} - \ell\right) \geq 0$ (together with $|w_2| \leq 1$ for DEC). With $\ell = 10^{-1}$ and $K = 0.095$ one obtains $K\left(\frac{1}{3} - \ell\right) > 0$, hence all three conditions are satisfied pointwise; the radial decay is stronger and produces a sharper falloff at larger r.

The two panels illustrate the algebraic pattern: $K(1 - 2w_2 - \ell)$ controls the sign of NEC and DEC combinations, while the product $w_2 K(1 - 2w_2 - \ell)$ controls the SEC.

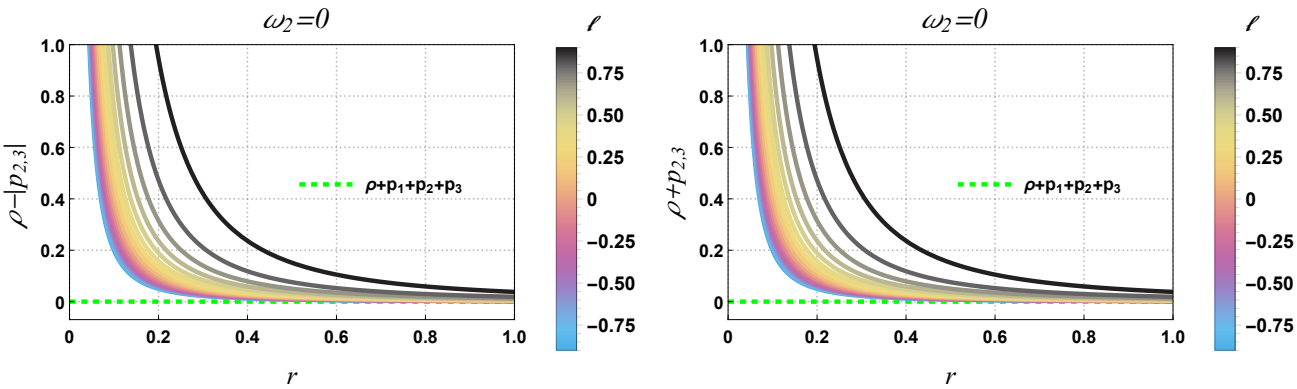

(a) [$K = 0.095$]. (b) [$K = 0.095$].

FIG. 2: The variation of $\rho + \sum_i p_i$ (strong energy condition), $\rho + p_{2,3}$ (null energy condition), and $\rho - \mid p_{2,3} \mid$ (dominant energy condition) against r for various values of ℓ with $w_2 = 0$.

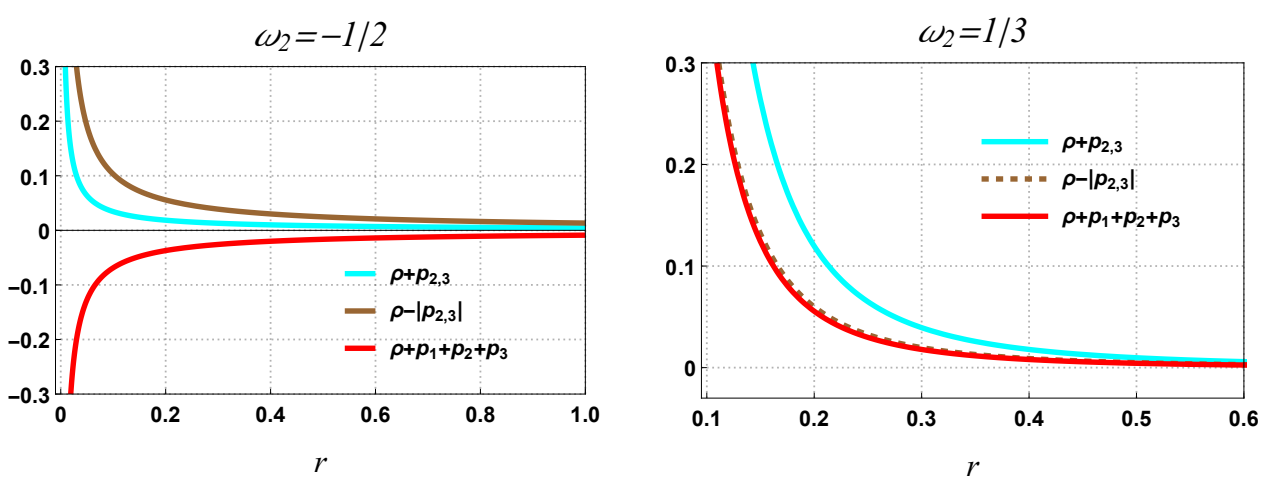

(a) [$K = 0.095$, $\ell = 0.1$]. (b) [$K = 0.095$, $\ell = 0.1$].

FIG. 3: The variation of $\rho + \sum_i p_i$ (strong energy condition), $\rho + p_{2,3}$ (null energy condition), and $\rho - \mid p_{2,3} \mid$ (dominant energy condition) against r for $w_2 = -1/2$ (left) and $w_2 = 1/3$ (right).

III. GEODESIC MOTIONS: NULL GEODESIC

This section examines the geodesic motion of test particles within the spacetime of an anisotropic fluid black hole in KR gravity. We focus on how the KR field parameter and the surrounding fluid density influence particle trajectories

and light deflection. The study of geodesic motion is essential for understanding BH properties, as it provides insights into spacetime geometry and observable phenomena such as gravitational lensing and BH shadows [84–87]. Analyzing the paths of particles and light is also crucial for interpreting high-energy astrophysical processes. We will use the Lagrangian approach to investigate this motion [88–92].

The Lagrangian density for the given metric is presented as the starting point for this analysis.

$$\mathcal{L} = \frac{1}{2}\left[-f(r)\left(\frac{dt}{d\tau}\right)^2 + \frac{1}{f(r)}\left(\frac{dr}{d\tau}\right)^2 + r^2\left(\frac{d\phi}{d\tau}\right)^2\right], \tag{41}$$

where τ represents an affine parameter and the geodesic motion in the equatorial plane $\theta = \pi/2$.
Since the chosen spacetime is static and spherically symmetric, it admits two Killing vector fields: the energy E and the angular momentum L of test particles, which are given by

$$\mathrm{E} = f(r)\left(\frac{dt}{d\tau}\right) \quad , \quad \mathrm{L} = r^2\,\frac{d\phi}{d\tau}. \tag{42}$$

After substituting Eq. (42) into Eq. (41), we obtain the equation of motion associated with the radial coordinate r.

$$\left(\frac{dr}{d\tau}\right)^2 + V_{\rm eff}(r) = \mathrm{E}^2 \tag{43}$$

which is equivalent to the one-dimensional equation of motion of a unit mass particle having energy E^2 and the potential $V_{\rm eff}(r)$. The effective potential governing the dynamics of test particles around the BH is given by

$$V_{\rm eff}(r) = \left(\varepsilon + \frac{\mathrm{L}^2}{r^2}\right)\left(\frac{1}{1-\ell} - \frac{2M}{r} - \frac{K}{1-\ell}\,r^{\frac{2w_2}{\ell-1}}\right). \tag{44}$$

Here $\varepsilon = 0$ for null geodesics and 1 for time-like geodesics.

A. Null Geodesic

The study of null geodesics is essential for understanding black hole physics and their observable features, like the photon sphere and shadow. The effective potential is a key tool for this analysis, as it describes how light behaves in the curved spacetime near a black hole. In the null geodesic case, $\varepsilon = 0$, the effective potential from Eq. (44) becomes:

$$V_{\rm eff}(r) = \frac{\mathrm{L}^2}{r^2}\left(\frac{1}{1-\ell} - \frac{2M}{r} - \frac{K}{1-\ell}\,r^{\frac{2w_2}{\ell-1}}\right). \tag{45}$$

Here, we study the dynamics of photons in a gravitational field and show how various parameters affect their effective radial force near a BH. Using the effective potential given in Eq. (45), we can determine the effective radial force on as,

$$\mathrm{F}_{\rm ph} = -\frac{1}{2}\frac{dV_{\rm eff}}{dr} = \frac{\mathrm{L}^2}{r^3}\left(\frac{1}{1-\ell} - \frac{3\,M}{r} - \frac{K(1+w_2)}{(1-\ell)r^{2w_2}}\right). \tag{46}$$

We see that the effective radial force experienced by the photon particles is influenced by the KR parameter ℓ, the fluid density parameter K, the conserved angular momentum L and the BH mass M. In the limit where $K = 0$, the above result (46) reduces to that of the Schwarzschild BH solution in KR gravity, which further simplifies to the standard Schwarzschild BH result when $\ell = 0$.

B. Photon sphere and BH shadow

This subsection analyzes the combined impact of KR gravity and an anisotropic fluid on key features of photon dynamics: the photon sphere and shadow radius.

Case	Effective Radial Force
$w_2 = 0$ (Dust)	$\frac{L^2}{r^3}\left(\frac{1}{1-\ell} - \frac{3\,M}{r} - \frac{K}{1-\ell}\right)$
$w_2 = 1/3$ (Radiation)	$\frac{L^2}{r^3}\left(\frac{1}{1-\ell} - \frac{3\,M}{r} + \frac{K(3\ell-4)}{3(1-\ell)^2} r^{2/3(\ell-1)}\right)$
$w_2 = -1/2$ (Dark Energy-like)	$\frac{L^2}{r^3}\left(\frac{1}{1-\ell} - \frac{3\,M}{r} + \frac{K(2\ell-1)}{2(1-\ell)^2} r^{1/(1-\ell)}\right)$.

TABLE I: Effective radial force under values of the equation-of-state parameter.

Circular null geodesics require the conditions $\dot{r} = 0$ and $\ddot{r} = 0$. This leads to the following two relationships:

$$E^2 = V_{\rm eff}(r) = \frac{L^2}{r^2}\, f(r) \quad , \quad \frac{dV_{\rm eff}(r)}{dr} = 0. \tag{47}$$

The first relation in Eq. (47) gives us the critical impact parameter for photons. The second relation $\frac{dV_{\rm eff}(r)}{dr} = 0$ gives us the photon sphere radius $r = r_{\rm ph}$ satisfying the following equation:

$$2\, f(r) = r\, f'(r) \Rightarrow 6(1-\ell)^2 M - 2r\left(1 - \ell + K(\ell - 1 - w_2) r^{2w_2/(\ell-1)}\right) = 0. \tag{48}$$

When the parameters are set to $K = 0$ and $\ell = 0$, Eq. (48) simplifies to $3M$. The solution of Eq. (48) depends on the choice of the equation-of-state parameter w_2. Analytically, we obtain the photon sphere radius for three distinct values of the equation-of-state parameter as follows:

Case I: $w_2 = 0$ **(Dust)** The photon sphere equation (48) becomes

$$(1-K)r - 3(1-\ell)M = 0 \quad \Rightarrow \quad r_{ph} = \frac{3\,M(1-\ell)}{1-K}. \tag{49}$$

Case II: $w_2 = \frac{1}{3}$ **(Radiation)** Equation (48) becomes

$$\left(1 - \ell + K(\ell - \frac{4}{3}) r^{2/3(\ell-1)}\right) r - 3(1-\ell)^2 M = 0. \tag{50}$$

For $0 < K < 1$, the photon sphere equation (50) reduces to a nonlinear algebraic equation with fractional powers. By introducing the variable $x = r^{1/3}$, the equation can be recast into a mixed-power polynomial form as

$$(1-\ell)x^3 + K(\ell - \frac{4}{3}) x^{2\ell+1} - 3(1-\ell)^2 M = 0. \tag{51}$$

Although no closed-form solution exists for generic ℓ, the equation admits a unique positive real root. Exact analytical solutions for the photon sphere radius are challenging. Thus, we attempted a numerical solution to determine the photon sphere radius.

Case III: $w_2 = -\frac{1}{2}$ **(Dark Energy-like)** Equation (48) becomes

$$\left(1 - \ell + K(\ell - \frac{1}{2}) r^{1/(1-\ell)}\right) r - 3(1-\ell)^2 M = 0. \tag{52}$$

Approximate solution of Eq. (52) is given by (see appendix)

$$r(K) \approx 3(1-\ell)M \; - \; \frac{\ell - \frac{1}{2}}{1-\ell}\left[3(1-\ell)M\right]^{\frac{2-\ell}{1-\ell}} K \; + \; \mathcal{O}(K^2) \tag{53}$$

Figure 4 shows three-dimensional visualizations of the photon sphere radius for three distinct values of the equation-of-state parameter w_2 as a function of the combined values of K and ℓ. Our analysis shows that raising both K and ℓ expands the photon sphere r_{ph}.

Next, we continue computing the black hole shadow, the dark image formed by photons trapped near unstable circular orbits at the photon sphere. Its measurable radius R_s is determined by the critical impact parameter b_c, which depends on the spacetime geometry. The BH shadow, as observed by a static observer at radial position r_O, has an apparent radius given by [93]

$$R_{\rm sh} = r_{\rm ph}\sqrt{\frac{f(r_O)}{f(r_{\rm ph})}} = r_{\rm ph}\sqrt{\frac{\frac{1}{1-\ell} - \frac{2M}{r_O} - \frac{K}{1-\ell}\, r_O^{\frac{2w_2}{\ell-1}}}{\frac{1}{1-\ell} - \frac{2M}{r_{\rm ph}} - \frac{K}{1-\ell}\, r_{\rm ph}^{\frac{2w_2}{\ell-1}}}}. \tag{54}$$

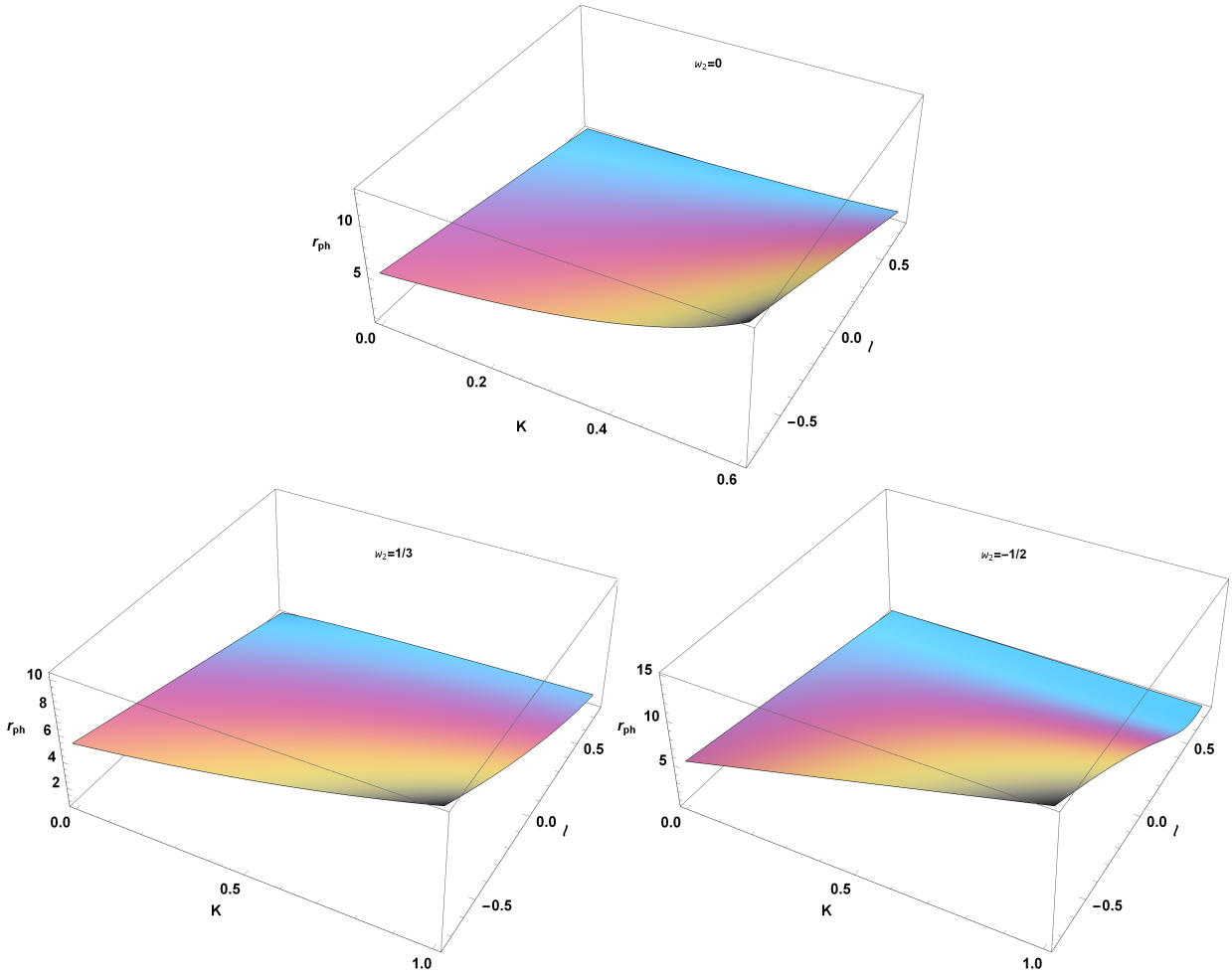

FIG. 4: Plot of the photon sphere r_{ph} vs K and ℓ and for certain values of w_2, dust (Top), Radiation (middle), and dark energy-like (bottom). Here, $M = 1$.

Analytically, the shadow radius for three distinct values of the equation-of-state parameter is :
Case I: $w_2 = 0$ **(Dust)**

$$R_{\rm sh} = r_{\rm ph}\sqrt{\frac{\frac{1}{1-\ell} - \frac{2M}{r_O} - \frac{K}{1-\ell}}{\frac{1}{1-\ell} - \frac{2M}{r_{\rm ph}} - \frac{K}{1-\ell}}} \tag{55}$$

For a distant observer ($r_O \to \infty$), the shadow radius simplifies to

$$R_{\rm sh} = r_{\rm ph}\sqrt{\frac{\frac{1-K}{1-\ell}}{\frac{1}{1-\ell} - \frac{2M}{r_{\rm ph}} - \frac{K}{1-\ell}}}\,. \tag{56}$$

Case II: $w_2 = \frac{1}{3}$ **(Radiation)**

$$R_{\rm sh} = r_{\rm ph}\sqrt{\frac{\frac{1}{1-\ell} - \frac{2M}{r_O} - \frac{K}{1-\ell}\, r_O^{\frac{2}{3(\ell-1)}}}{\frac{1}{1-\ell} - \frac{2M}{r_{\rm ph}} - \frac{K}{1-\ell}\, r_{\rm ph}^{\frac{2}{3(\ell-1)}}}}\,. \tag{57}$$

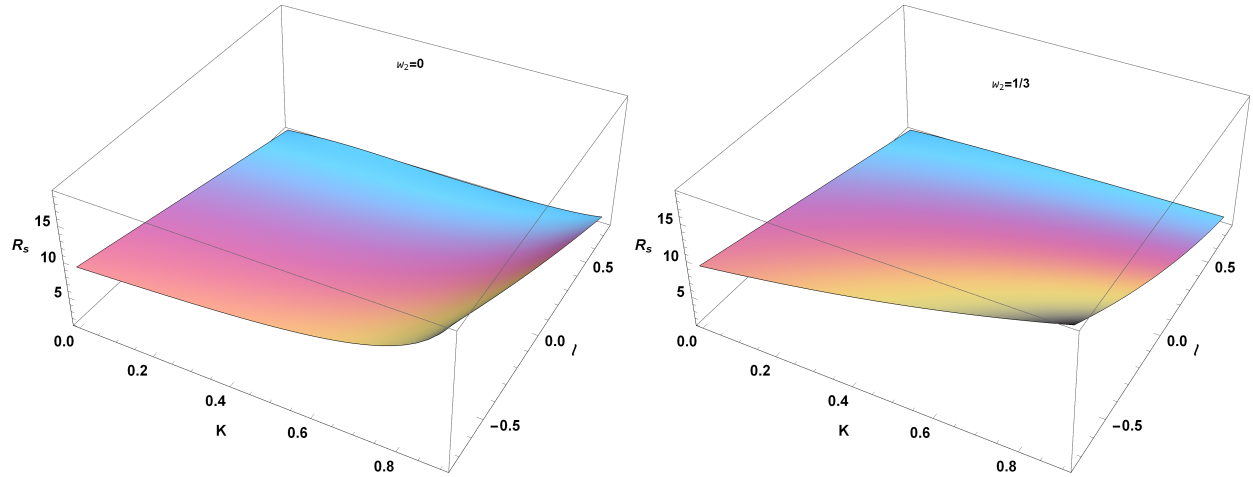

FIG. 5: Plot of the shadow radius R_s vs K and ℓ and for certain values of w_2, Dust (left) and Radiation (right). Here, $M = 1$.

For a distant observer ($r_O \to \infty$) and $-1 < \ell < 1$, the shadow radius simplifies to

$$R_{\rm sh} = r_{\rm ph}\sqrt{\frac{\frac{1}{1-\ell}}{\frac{1}{1-\ell} - \frac{2M}{r_{\rm ph}} - \frac{K}{1-\ell}\, r_{\rm ph}^{\frac{2}{3(\ell-1)}}}}. \tag{58}$$

Case III: $w_2 = -\frac{1}{2}$ **(Dark Energy-like)**

$$R_{\rm sh} = r_{\rm ph}\sqrt{\frac{\frac{1}{1-\ell} - \frac{2M}{r_O} - \frac{K}{1-\ell}\, r_O^{\frac{1}{1-\ell}}}{\frac{1}{1-\ell} - \frac{2M}{r_{\rm ph}} - \frac{K}{1-\ell}\, r_{\rm ph}^{\frac{1}{1-\ell}}}}. \tag{59}$$

For a distant observer ($r_O \to \infty$), the shadow radius $R_{\rm sh} =$ Undefined.

Figure 5 shows three-dimensional visualizations of the shadow radius for two distinct values of the equation-of-state parameter w_2 as a function of the combined values of K and ℓ. The figure shows that the shadow radius increases with both parameters K and ℓ.

At this stage, we constrain the model parameters ℓ and K by using the shadow data from the EHT observations of M87* and Sgr A* [71, 94–98]. We also take into account the observational uncertainties reported in Refs. [99, 100]. Since the shadow size is directly related to the photon sphere, these observations provide a strong test for gravitational models in the strong-field regime.

For the comparison with the EHT results, we recall that the theoretical shadow diameter is defined as $d_{\rm sh}^{\rm theo} = 2R_{\rm sh}$. In our analysis, this quantity is dimensionless because the radial coordinate is scaled by the black hole mass M. On the observational side, the shadow diameter is given by [101]

$$d_{\rm sh} = \frac{D\theta_*}{\gamma M_\odot}, \tag{60}$$

where D is the distance to the source in parsecs, θ_* is the measured angular diameter, and γ is the mass of the black hole in units of the solar mass.

For M87* we use $\gamma = (6.5 \pm 0.90) \times 10^9$ and $D = 16.8\,$Mpc [94], while for Sgr A* we take $\gamma = (4.3 \pm 0.013) \times 10^6$ and $D = 8.127\,$kpc [97]. The measured angular diameters are $\theta_* = (42 \pm 3)\,\mu$as for M87* and $\theta_* = (48.7 \pm 7)\,\mu$as for Sgr A*. Substituting these values into Eq. (60), we obtain $d_{\rm sh}^{\rm M87*} = (11 \pm 1.5)$ and $d_{\rm sh}^{\rm SgrA*} = (9.5 \pm 1.4)$.

These constraints at the 1σ level are used in Fig. 6 to determine the allowed regions in the (ℓ, K) plane for the representative cases $w_2 = 0$ and $w_2 = 1/3$. From the plots, one can see a clear dependence of the allowed region on both w_2 and the source. For $w_2 = 0$, the contours of constant $d_{\rm sh}^{\rm theo}$ are almost linear, and the allowed region has a wedge-like shape. This shows a near-linear degeneracy between ℓ and K, meaning that an increase in ℓ can

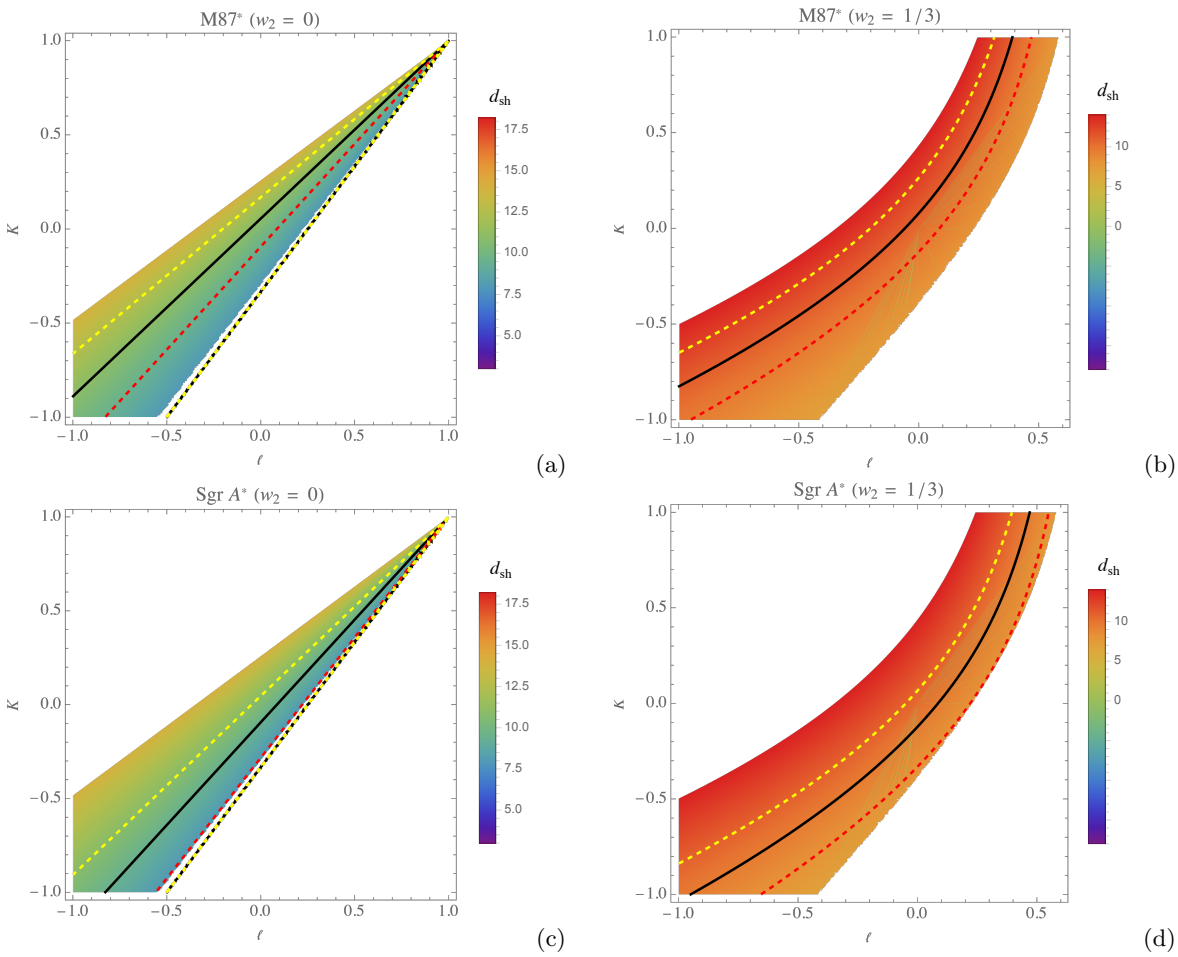

FIG. 6: The dependence of the model parameters ℓ and K in the context of the theoretical shadow diameter $d_{\rm sh}^{\rm theo}$, within the observational bounds for (a,b) M87* and (c,d) Sgr A*. The solid black curve represents the central value defined by $d_{\rm sh}^{\rm theo} = d_{\rm sh}$, whereas the red and yellow dashed curves correspond to the -1σ and $+1\sigma$ uncertainty levels, respectively.

be compensated by a larger K to keep the shadow size unchanged. This behaviour is similar for M87* and Sgr A*, although the width and slope of the bands are slightly different because of the different observational inputs. For $w_2 = 1/3$, the situation changes, and the contours become clearly curved. In this case, the degeneracy between ℓ and K is partially removed, and the shadow diameter becomes more sensitive to ℓ, especially for larger values of this parameter.

Comparing the two sources, the allowed region for Sgr A* is slightly narrower, which gives stronger bounds on the parameter combination. However, the degeneracy orientation is the same in both cases, indicating that the KR corrections affect the shadow in a universal way. In addition, larger values of $d_{\rm sh}^{\rm theo}$ are located toward the upper-right part of the parameter space, which means that both ℓ and K increase the shadow size, while the lower-left region is excluded by the EHT data. Hence, the case $w_2 = 1/3$ imposes stronger constraints, as it reduces the linear degeneracy among the parameters. The overlap between the allowed regions from M87* and Sgr A* indicates a common range of (ℓ, K) compatible with both observations, supporting the viability of the model and suggesting that a combined analysis can further tighten the bounds.

IV. WEAK DEFLECTION ANGLE

Gravitational lensing arises from the bending of light by the gravitational field of massive objects such as planets, black holes, or dark matter, a phenomenon predicted by Einstein's general relativity in the weak-field regime. In

particular, weak gravitational deflection plays a central role in observational astrophysics, as it is widely used to trace dark matter filaments and to probe the large-scale structure of the Universe. Among the available techniques to compute the weak deflection angle, a powerful geometric approach was developed by Gibbons and Werner, based on the Gauss–Bonnet theorem applied to the optical metric [102, 103]. Within this framework, the bending of light can be interpreted as a global geometric (partly topological) effect, and the deflection angle is obtained by integrating the Gaussian curvature of the optical manifold outside the photon trajectory. Thanks to its geometric formulation, this method has been widely used in many lensing scenarios [104–115]).

In this subsection, we pursue the approach in Refs. [116, 117], which introduces a method to calculate the light bending angle for non-asymptotically flat spacetimes.

For null geodesics ($ds^2 = 0$), the optical metric is defined by

$$dt^2 = \bar{g}_{ij} dx^i dx^j, \tag{61}$$

which yields

$$d\sigma^2 = \frac{dr^2}{f(r)^2} + \frac{r^2}{f(r)} d\phi^2. \tag{62}$$

This two-dimensional Riemannian geometry fully encodes light propagation. In such a case, the Gaussian curvature associated with the optical metric is obtained as

$$\mathcal{K} = -\frac{1}{r} f(r)\sqrt{f(r)}\, \frac{d}{dr}\left[f(r) \frac{d}{dr}\left[\frac{r}{\sqrt{f(r)}} \right] \right], \tag{63}$$

which can be approximated as

$$\mathcal{K} = -\frac{2M}{r^3} - \frac{K}{2(1-\ell)} \nu(\nu-1) r^{\nu-2} + \mathcal{O}(M^2, K^2, MK), \tag{64}$$

where we have defined

$$\nu \equiv \frac{2w_2}{\ell - 1}. \tag{65}$$

The expression (64) is essentially what is needed to apply the Gauss-Bonnet theorem used in Refs. [116, 117]. We consider the quadrilateral domain $\mathcal{D}$ bounded by the photon trajectory γ, a radial geodesic from the source S at r_S, and a radial geodesic from the observer O at r_O, a circular arc C_R of radius R, which will be shrunk away. The Gauss-Bonnet theorem then gives

$$\iint_{\mathcal{D}} \mathcal{K}\, d\mathcal{S} + \int_\gamma \kappa_g dl + \sum_i \theta_i = 2\pi, \tag{66}$$

where κ_g is the geodesic curvature of the light ray boundary curve with respect to the optical metric, and along the photon trajectory, we have $\kappa_g = 0$. After careful evaluation, the finite-distance deflection angle is [117]

$$\hat{\alpha} = -\iint_{\mathcal{D}} \mathcal{K}\, d\mathcal{S} + \Psi_O + \Psi_S - \pi, \tag{67}$$

in which Ψ_O is the angle between the photon trajectory and the radial direction at the observer, and Ψ_S is the corresponding angle at the source.

The surface element of the optical metric is

$$d\mathcal{S} = \sqrt{\det[\bar{g}]}\, dr\, d\phi = \frac{r}{f(r)^{3/2}}\, dr\, d\phi. \tag{68}$$

To leading-order, the photon trajectory is approximated by

$$r(\phi) \simeq \frac{b}{\sin\phi}, \tag{69}$$

where the impact parameter $b \equiv \mathrm{L/E}$, is defined at the point of closest approach as

$$b^2 = \frac{r_0^2}{f(r_0)}, \tag{70}$$

which remains well-defined without asymptotic flatness. The radial integration is therefore bounded by

$$r(\phi) \leq r \leq r_O \quad \text{(observer side)}, \qquad r(\phi) \leq r \leq r_S \quad \text{(source side)}. \tag{71}$$

Now, splitting the domain at the point of closest approach, the curvature contribution becomes

$$\hat{\alpha}_{\mathcal{K}} = -\int_0^{\phi_O} \int_{b/\sin\phi}^{r_O} \mathcal{K}\, d\mathcal{S} - \int_{\phi_O}^{\pi} \int_{b/\sin\phi}^{r_S} \mathcal{K}\, d\mathcal{S}. \tag{72}$$

We now evaluate this explicitly.

Using the expression in Eq. (64), one gets the contribution of the Schwarzschild part to the deflection angle as

$$\hat{\alpha}_M = \int \frac{2M}{r^3} \frac{r}{f_0^{3/2}}\, dr\, d\phi, \tag{73}$$

where $f_0 = 1/(1-\ell)$. This yields

$$\hat{\alpha}_M = \frac{2M}{f_0^{3/2}} \left[\int_0^{\phi_O} \left(\frac{1}{b/\sin\phi} - \frac{1}{r_O} \right) d\phi + \int_{\Phi_O}^{\pi} \left(\frac{1}{b/\sin\phi} - \frac{1}{r_S} \right) d\phi \right]. \tag{74}$$

This integral can be calculated directly, yielding

$$\hat{\alpha}_M = \frac{2M}{b} f_0^{-3/2} \left(\sin\phi_O + \sin\phi_S \right) - 2M f_0^{3/2} \left(\frac{\phi_O}{r_O} + \frac{\pi + \phi_O}{r_S} \right). \tag{75}$$

Now the local angles at the source and observer satisfy the relations

$$\sin\Psi_O = \frac{b\sqrt{f(r_O)}}{r_O}, \qquad \sin\Psi_S = \frac{b\sqrt{f(r_S)}}{r_S}. \tag{76}$$

Geometrically this means

$$\phi_O = \pi - \Psi_O, \qquad \phi_S = \Psi_S. \tag{77}$$

Accordingly, the total deflection angle is given by

$$\hat{\alpha} = \hat{\alpha}_M + \hat{\alpha}_K + \Psi_O + \Psi_S - \pi. \tag{78}$$

Now to calculate the contribution of the dark matter, i.e., the K-term, we use the second term of Eq. (64), which gives

$$\hat{\alpha}_k = \frac{f_0}{2} K(\nu - 1) \left\{ \int_0^{\phi_0} \left[\left(\frac{b}{\sin\phi} \right)^{\nu} - r_O^{\nu} \right] d\phi + \int_{\phi_0}^{\pi} \left[\left(\frac{b}{\sin\phi} \right)^{\nu} - r_S^{\nu} \right] d\phi \right\}. \tag{79}$$

For the case of a universe filled with dust (i.e. $w_2 = 0$ or $\nu = 0$), this integral provides, after manipulations

$$\hat{\alpha}_K^{\text{dust}} = -\frac{\pi}{2} K f_0. \tag{80}$$

For the radiation case (i.e. $w_2 = 1/3$ or $\nu = 2f_0/3$), the integral in Eq. (79), provides

$$\hat{\alpha}_K^{\text{rad}} = \frac{f_0}{2} K(\nu - 1) \left[b^{\nu} \sqrt{\pi} \frac{\Gamma\left(\frac{1-\nu}{2}\right)}{\Gamma\left(\frac{2-\nu}{2}\right)} - \left(\phi_O r_O^{\nu} + (\pi - \phi_O) r_S^{\nu} \right) \right], \tag{81}$$

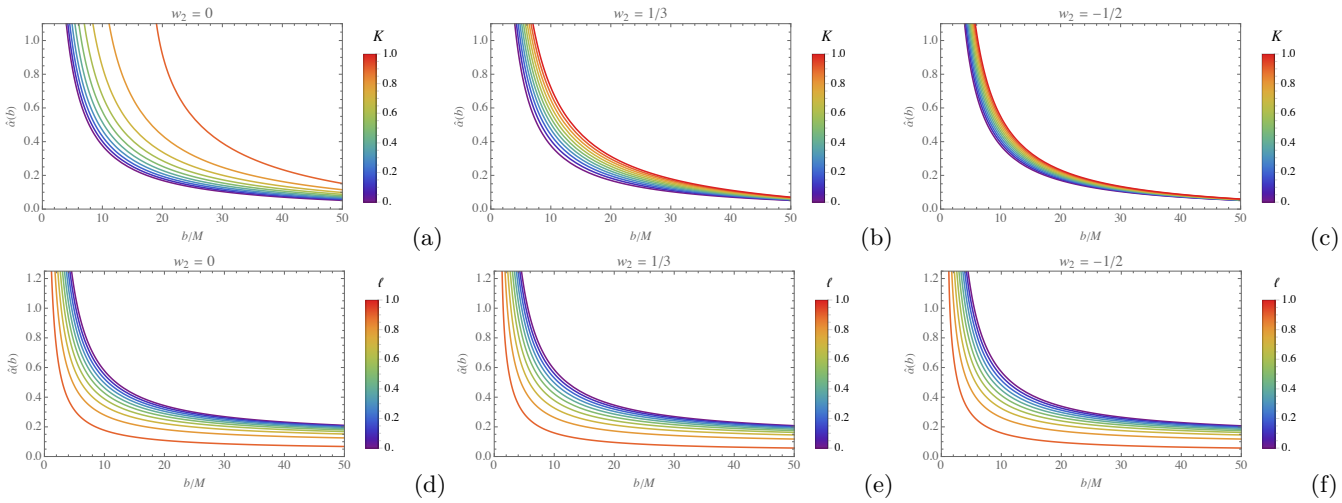

FIG. 7: The b-profiles of the weak deflection angle $\hat{\alpha}(b)$ for the three values of w_2, evaluated at $r_O = r_S = 100M$. Panels (a–c) correspond to fixed $\ell = 0.1$ and varying K, while panels (d–f) show fixed $K = 0.1$ and varying ℓ.

to obtain which, we have used the identity

$$\int_0^{\pi} \sin^{-\nu}\phi \, d\phi = \sqrt{\pi}\,\frac{\Gamma\left(\dfrac{1-\nu}{2}\right)}{\Gamma\left(\dfrac{2-\nu}{2}\right)}. \tag{82}$$

For a universe dominated by DE-like matter, characterized by $w_2 = -1/2$ or equivalently $\nu = f_0$, the same procedure applied to the master integral in Eq. (79) leads to an analytic expression identical to that obtained in Eq. (81). The distinction arises at the numerical level, where the appropriate value of ν must be implemented when generating the corresponding profiles.

In Fig. 8, we display several b-profiles of the weak deflection angle for the three considered values of w_2, allowing a direct comparison of the lensing behaviour across the different cosmological backgrounds. From the diagrams, it is clear that, in all configurations, the deflection angle decreases monotonically with increasing impact parameter b, while larger values K enhance the overall bending, consistently reflecting a stronger effective gravitational field. For dust ($w_2 = 0$), the curves show only a moderate spread, indicating a weak sensitivity of the deflection angle to both K and the KR parameter ℓ. This sensitivity becomes more pronounced for radiation ($w_2 = 1/3$), where the profiles are steeper at small b and the separation between curves increases, signaling a stronger interplay between geometry, matter content, and the ℓ spectrum. The DE-like case ($w_2 = -1/2$) exhibits the largest deviations, with both K and ℓ producing a significant enhancement of the deflection angle over a wide range of impact parameters, particularly in the strong-lensing regime. Thus, while the qualitative behaviour of $\hat{\alpha}(b)$ is universal, its magnitude and parametric sensitivity grow as one moves from dust to radiation and finally to DE-dominated backgrounds.

V. GRAVITATIONAL LENSING IN SDL

In this section, we investigate strong gravitational lensing by an anisotropic fluid black hole within the Kalb-Ramond gravity framework. Specifically, we analyse the trajectory of light rays in the equatorial plane and examine how the black hole parameters influence the lensing observables in SDL, where the closest approach distance r_0 approaches the photon sphere radius $r_{\rm ph}$. In this regime, the deflection angle increases monotonically, exceeding 2π radians and diverging logarithmically as $r_0 \to r_{\rm ph}$ [65].

For a photon propagating on the equatorial plane of a static and spherically symmetric spacetime, the bending of light is characterized by the deflection angle $\alpha_D(r_0)$, defined as the angle between the asymptotic incoming and outgoing directions. As a function of the closest approach distance r_0, it is given by [65, 118–121]:

$$\alpha_D(r_0) = I(r_0) - \pi, \tag{83}$$

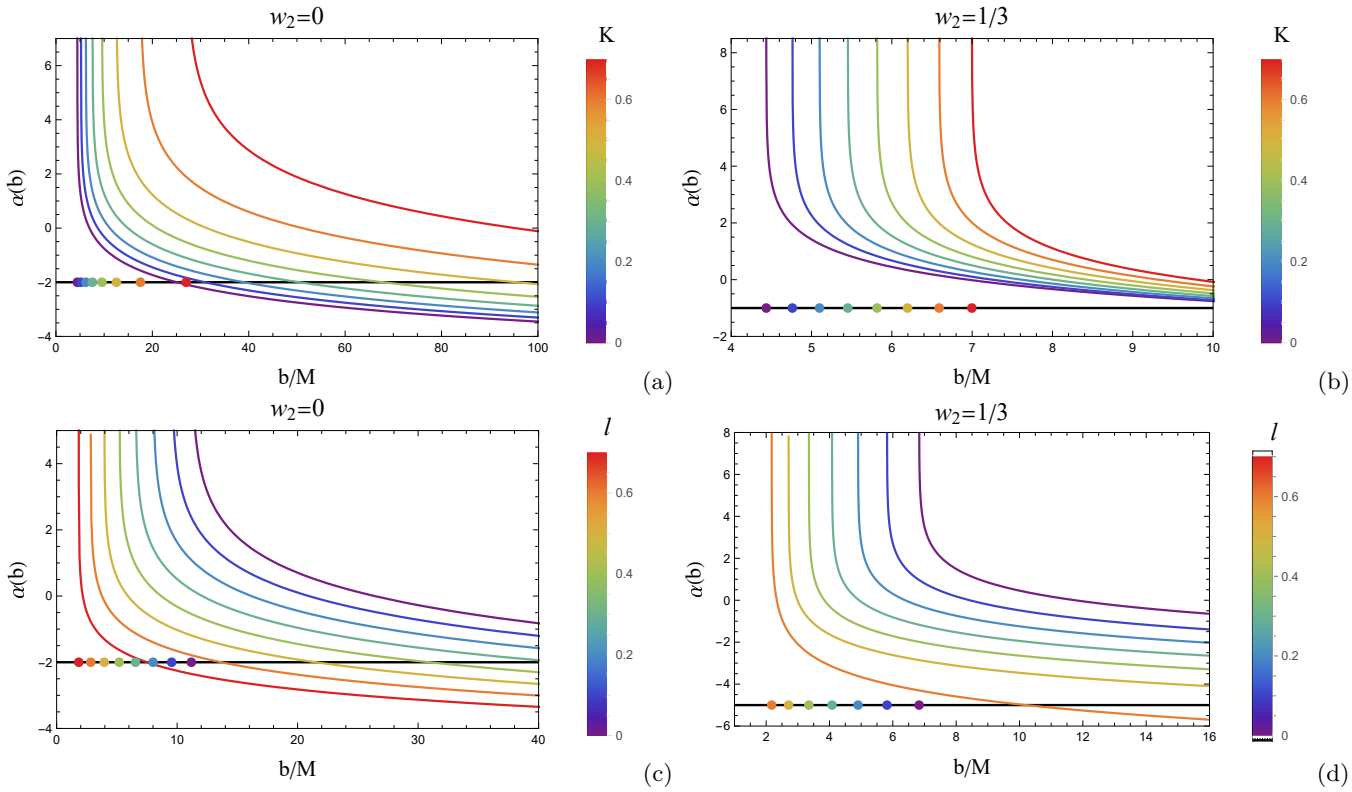

FIG. 8: The deflection angle as a function of b for two values of w_2. Panels (a–b) correspond to fixed $\ell = 0.1$ and varying K, while panels (c–d) show fixed $K = 0.4$ and varying ℓ. Here, the dots on the black solid line correspond to the values of the critical impact parameter where $\alpha(b)$ diverges.

where $I(r_0)$ represents the total azimuthal angle traversed by the photon from its point of closest approach to infinity. Using the geodesic equations (42) and (43), we can find an explicit expression for the integral $I(r_0)$ in terms of metric coefficients. Since the integral cannot be solved explicitly, the integral is expanded near the unstable photon sphere radius [63, 65] by defining a new variable $z = 1 - r_0/r$ in SDL [122, 123]. The analytical expression of the deflection angle for spacetime (17) as a function of the impact parameter ($b \approx \theta D_{OL}$) is given by [65, 124, 125]

$$\alpha_D(b) \;=\; \bar{a}\log\left(\frac{b}{b_c} - 1\right) + \bar{b} + \mathcal{O}(b - b_c), \tag{84}$$

where $\bar{a}$, $\bar{b}$ are the strong lensing coefficients. Detailed calculations can be found in [65, 124, 125]. Figure 8 shows the deflection angle for an anisotropic fluid black hole in KR gravity, with $w_2 = 0$ (Dust) and $w_2 = 1/3$ (Radiation), for different values of the parameters l and K. For dust, we observe that the deflection angle diverges at larger values of the critical impact parameter than in the radiation case. In case of $w_2 = -1/2$ (Dark energy like), however, the critical impact parameter is not defined, as indicated in Eq. (59). As a result, strong deflection cannot occur from the perspective of a distant observer.

The theoretical framework for analyzing strong gravitational lensing in the vicinity of a black hole is completed by the lens equation, which relates the angular position of the source to the apparent positions of the resulting relativistic images. For a scenario where both the observer and the source are situated in an asymptotically flat spacetime region far from the lensing black hole, and are nearly perfectly aligned with it, the lens equation can be approximated as [65, 126]:

$$\beta = \theta - \frac{D_{LS}}{D_{OL} + D_{LS}}\Delta\alpha_n, \tag{85}$$

where β and θ denote the angular positions of the source and the image, respectively, measured from the optical axis (the line connecting the observer to the lens). The quantity $\Delta\alpha_n = \alpha(\theta) - 2n\pi$ represents the offset of the

deflection angle from the $2n\pi$ multiple required for the photon to loop around the black hole n times. In SDL, we have $0 < \Delta\alpha_n \ll 1$. Here, $D_{\rm LS}$ is the distance from the lens to the source plane, and $D_{\rm OL}$ is the distance from the observer to the lens, with the observer-source distance approximated as $D_{\rm OS} \approx D_{\rm OL} + D_{\rm LS}$.

Following Bozza [65, 127], we define three characteristic observables in SDL as

$$\theta_\infty = \frac{b_c}{D_{OL}}, \tag{86}$$

$$s = \theta_1 - \theta_\infty \approx \theta_\infty \exp\left(\frac{\bar{b}}{\bar{a}} - \frac{2\pi}{\bar{a}}\right), \tag{87}$$

$$r_{\rm mag} = \frac{\mu_1}{\sum_{n=2}^{\infty}\mu_n} \approx \frac{5\pi}{\bar{a}\,\log(10)}. \tag{88}$$

In the above expression, θ_∞ is the asymptotic angular distance of the image distance, s is the angular separation between θ_1 and θ_∞, and $r_{\rm mag}$ is the ratio of the flux of the first image to that of all other images. Note that the observable $r_{\rm mag}$ does not depend on the distance between the observer and the lens D_{OL}, making it a direct probe of the spacetime geometry in the strong-field regime. By measuring these three quantities—θ_∞, s, and $r_{\rm mag}$ one can, in principle, reconstruct the black hole metric parameters and distinguish between different gravitational theories.

VI. ANALYSIS OF LENSING OBSERVABLES FOR SUPERMASSIVE BLACK HOLES

In this section, we apply the formalism from the previous section to numerically estimate lensing observables in SDL by treating Sgr A* and M87* as anisotropic fluid black holes in KR gravity, using the parameters inferred from EHT observations. Using the latest astronomical observation data, the estimated mass and distance from the Earth of the M87* is given as $(6.5 \pm 0.7) \times 10^9 M_\odot$, and $d = 16.8$ MPc [128], respectively. Similarly. the estimated mass and distance of SgrA* is given as $4^{+1.1}_{-0.6} \times 10^6 M_\odot$, and $d = 8.15 \pm 0.15$ KPc [129].

We compare the relativistic image positions θ_∞ and lensing observables, s and r_{mag}, for an anisotropic fluid black hole in KR gravity with those for the Schwarzschild black hole. The results are summarized in Table II. We see that as we increase the KR coupling parameter l, the observable θ_∞ and s decrease while $r_{\rm mag}$ increases. Furthermore, the deviations in these quantities with respect to changes in l and K are more pronounced for the dust case ($w_2 = 0$) than for the radiation case ($w_2 = 1/3$). However, it is important to note that these strong deflection observables cannot be defined for the $w_2 = -1/2$ case (dark energy-like).

A. Constraints from EHT

The EHT campaign revealed a bright, asymmetric emission ring around M87 with an angular diameter $\theta_{sh} = 42 \pm 3$ μas, exhibiting a central brightness depression—the characteristic shadow signature—and constraining the ring's fractional width to < 0.5 [94, 95, 130]. Subsequent analysis of Sgr A* from the same observing campaign, released in 2022, similarly confirmed a ring-like structure with a diameter of 51.8 ± 2.3 μas [97]. By combining multiple imaging techniques—including EHT Imaging, SMILI, and DIFMAP—the envelope of 1-σ for the angular diameter of Sgr A* shadow is constrained to $\theta_{sh} = 48.7 \pm 7$ μas [71]. Despite M87* being approximately 1500 times more massive and 2000 times more distant than Sgr A*, their shadow diameters appear remarkably similar in the sky, making them ideal laboratories for testing gravity theories [84, 123, 131–136]

Taking the angular radius of the image position (θ_∞) as the angular size of the black hole shadow, the shadow diameter is defined as $\theta_{\rm sh} = 2\theta_\infty$. By modelling M87* and Sgr A* as an anisotropic fluid black hole within the Kalb-Ramond gravity framework, we can then place observational constraints on the deviation parameters l and K for different values of the equation-of-state parameter w_2. This is achieved by requiring that the theoretically predicted shadow diameter falls within the 1-σ observational bounds reported by the EHT for each supermassive black hole.

a. Constraints from Sgr A:* The observed average bounds for the shadow size of Sgr A * $\theta_{\rm sh} \in (46.9, 50)$ μas and the full 1-σ interval as $\in (41.7, 55.6)$ μas [71] in Fig. 9. The dashed black and solid red lines correspond to $\theta_{\rm sh} = 55.6\mu$as and $\theta_{\rm sh} = 41.7\mu$as, respectively. For dust ($w_2 = 0$), the 1-σ bound is given as - $0 \geq l \geq 0.065$ and $0 \geq K \geq 0.04$, while for radiation ($w_2 = 1/3$), bound is - $0.65 \geq K \geq 0.85$ and no constraint on the parameter l. Within this parameter range, the anisotropic fluid black hole in KR gravity is consistent with observations of the Sgr A* black hole shadow from the EHT.

TABLE II: Numerical estimation of strong lensing observables for supermassive black holes Sgr A* and M87*, as an anisotropic fluid black hole in KR gravity. We compare these observables with those for Schwarzschild black holes.

			Sgr A*		M87*		
w_2	l	K	$\theta_\infty(\mu\text{as})$	$s(\mu\text{as})$	$\theta_\infty(\mu\text{as})$	$s(\mu\text{as})$	r_{mag}
(GR)	0	0.0	26.39	0.32	19.33	0.233	6.24
0 (Dust)	0.2	0.0	18.840	0.00775	14.155	0.00582	7.627
	0.2	0.2	26.330	0.03295	19.782	0.02476	6.822
	0.2	0.4	40.537	0.17933	30.456	0.13474	5.908
	0.2	0.6	74.472	1.4732	55.952	1.1069	4.824
	0.2	0.8	210.64	29.345	158.26	22.047	3.411
	0.4	0.0	12.237	0.00099	9.194	0.00074	8.807
	0.4	0.2	17.102	0.00498	12.849	0.00374	7.877
	0.4	0.4	26.330	0.03295	19.782	0.02476	6.822
	0.4	0.6	48.371	0.34129	36.342	0.25641	5.570
	0.4	0.8	136.81	3.939	102.79	6.9078	9.1943
	0.6	0.0	6.661	3.49×10^{-5}	5.005	2.62×10^{-5}	10.786
	0.6	0.2	9.309	0.000235	6.994	0.000176	9.648
	0.6	0.4	14.332	0.002157	10.768	0.001621	8.355
	0.6	0.6	26.330	0.03295	19.782	0.02476	6.822
	0.6	0.8	74.472	1.4732	4.824	55.952	1.1069
1/3 (Radiation)	0.2	0.0	18.8401	0.00775148	14.1549	0.00582381	7.6271
	0.2	0.2	21.6894	0.0101109	16.2956	0.0075965	7.20685
	0.2	0.4	24.8362	0.0149536	18.6598	0.0112349	6.756
	0.2	0.6	28.3439	0.0233588	21.2952	0.0175498	6.2867
	0.2	0.8	32.2611	0.0376766	24.2383	0.028307	5.80704
	0.4	0	12.237	0.000986	9.19	0.00074	8.807
	0.4	0.2	14.314	0.00165	10.754	0.00124	7.9443
	0.4	0.4	16.97	0.0049	12.75	0.0037	6.738
	0.4	0.6	20.509	0.0221	15.409	0.0166	5.218
	0.4	0.8	25.186	0.1341	18.923	0.1007	3.209
	0.6	0	6.6609	3.48×10^{-5}	5.0045	2.61×10^{-5}	10.78
	0.6	0.2	8.238	9.74×10^{-5}	6.18	7.320×10^{-5}	9.354
	0.6	0.4	11.013	0.00602	8.27	0.00452	5.331

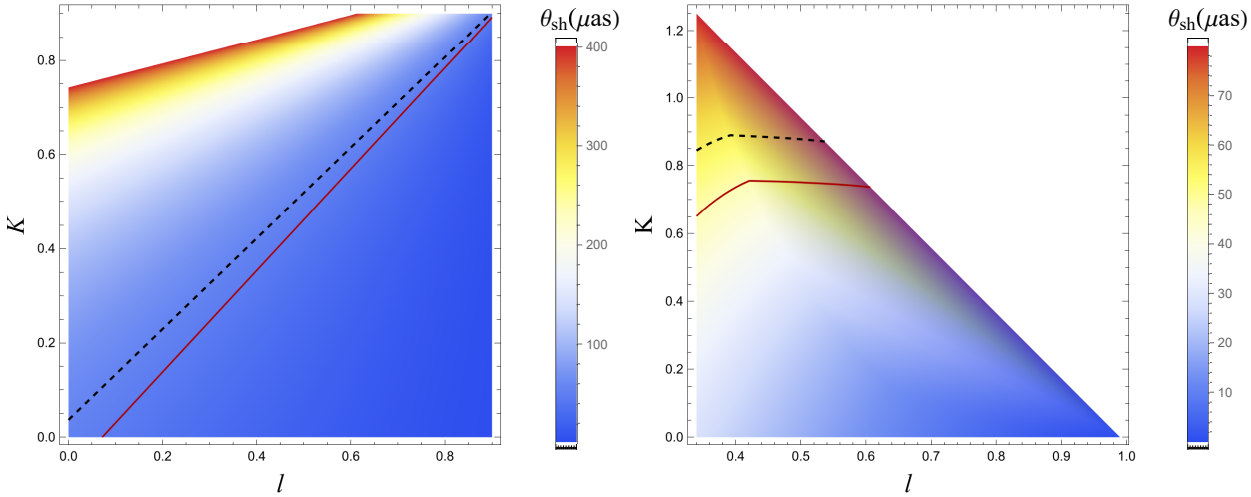

FIG. 9: Shadow angular diameter $\theta_{\text{sh}}(= 2\theta_\infty)$ as a function of parameters l and K for Dust $w_2 = 0$ (Left) and Radiation $w_2 = 1/3$ (Right), when Sgr A* is modelled as anisotropic fluid black hole in KR gravity. The dashed black and solid lines correspond to $\theta_{\text{sh}} = 55.6$ and $\theta_{\text{sh}} = 41.7$, respectively. The region between these lines satisfies the Sgr A* shadow 1-σ bound.

b. Constraints from M87:* In Fig. 10, the angular diameter $\theta_{\rm sh}$ is shown as a function of l and K for the M87* black hole. Given the offset of $\approx 10\%$ between the emission ring and the angular shadow diameter, we get the angular diameter of shadow to be within the range $\in (35.1, 40.5)$ μas [86, 94, 137] with an error of $\pm 2.7\%$ incorporating both measurement uncertainty and potential offset. Figure 10, the angular diameter $\theta_{\rm sh}$ for the for an anisotropic fluid black hole in KR gravity as M87* where dashed black and solid lines correspond to $\theta_{\rm sh} = 40.5$ and $\theta_{\rm sh} = 35.1$, respectively. In Fig. 10, the angular diameter $\theta_{\rm sh}$ is shown as a function of $\kappa\eta^2$ and γ for the M87* black hole. The bounds for dust ($w_2 = 0$) are $0.15 < l < 0.23$ and unbound for K, while for radiation ($w_2 = 1/3$), the bounds are $0.29 < K < 0.45$ and unbound for l.

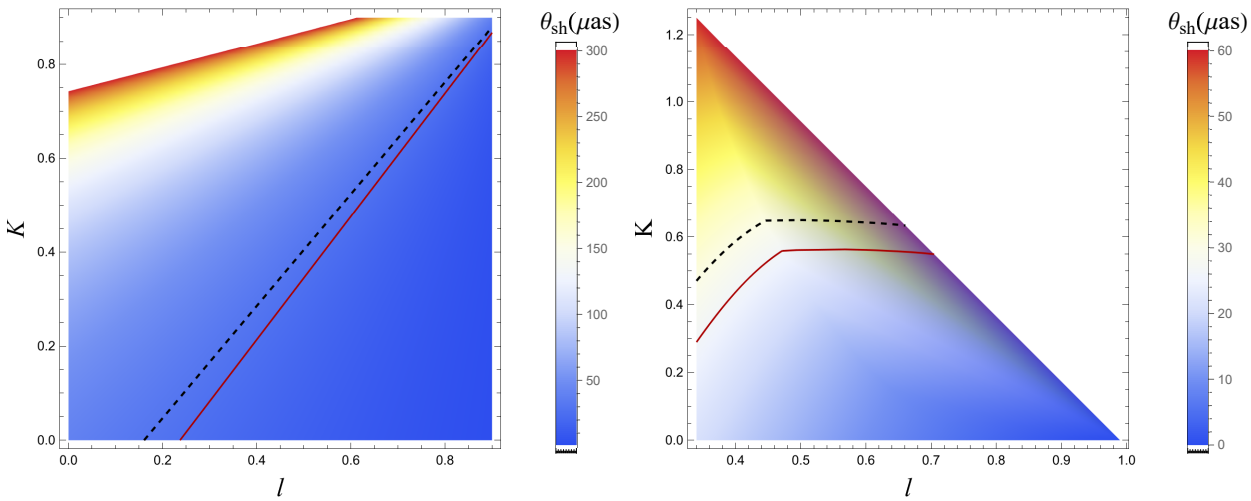

FIG. 10: Shadow angular diameter $\theta_{\rm sh}(= 2\theta_\infty)$ as a function of parameters l and K for Dust $w_2 = 0$ (Left) and Radiation $w_2 = 1/3$ (Right), when M87* is modelled as anisotropic fluid black hole in KR gravity. Here, the dashed black and solid lines correspond to $\theta_{\rm sh} = 40.5$ and $\theta_{\rm sh} = 35.1$. The region within this line satisfies the M87* shadow 1-σ bound.

VII. CONCLUSION

In this paper, we have successfully constructed and analyzed a novel class of exact black hole solutions within a framework where gravity is non-minimally coupled to a background KR field and immersed in an anisotropic fluid. The presence of a non-zero vacuum expectation value of the KR field triggers spontaneous Lorentz symmetry breaking, which, when combined with the anisotropic matter distribution, profoundly modifies the underlying spacetime geometry. Our comprehensive analysis yields several significant physical insights. Firstly, we found that the spacetime admits a rich horizon structure dictated by the KR coupling parameter ℓ and the fluid density parameter K. We established that the asymptotic behaviour and the satisfaction of the null, weak, strong, and dominant energy conditions depend strictly on the equation-of-state parameter w_2, where local repulsive behaviours (dark energy-like) induce severe violations of the strong energy condition while simultaneously extending the spatial influence of the black hole.

Furthermore, the critical parameters governing null geodesics, namely the photon sphere and the shadow radius, were derived analytically and explored numerically. We demonstrated that dark energy-like configurations ($w_2 = -1/2$) drastically alter the effective potential barrier, whereas dust ($w_2 = 0$) and radiation ($w_2 = 1/3$) backgrounds produce localised corrections to the Reissner–Nordström-like profile. We also analyzed the weak gravitational lensing in this spacetime using the Gauss–Bonnet method applied to the optical metric, which remains valid despite the non-asymptotically flat nature induced by the KR field and the surrounding anisotropic matter. The resulting deflection angle receives, in addition to the Schwarzschild-like term, corrections controlled by the fluid parameter K, the KR coupling ℓ, and the equation-of-state parameter w_2. In all considered cases, the deflection angle decreases with the impact parameter, while larger values of K and ℓ enhance the bending, with the strongest sensitivity appearing in the DE-like background.

Finally, we extended our optical analysis to the strong-field regime to extract measurable lensing observables, including the asymptotic angular position, image separation, and magnification ratio. Applying our model to the

supermassive black holes Sgr A* and M87*, we revealed quantifiable deviations from general relativity. Ultimately, this study bridges fundamental high-energy physics with observable astrophysics. The distinct lensing signatures and shadow modifications characterized here provide a concrete theoretical baseline for testing modified gravity and detecting anisotropic matter distributions, such as dark matter halos or scalar condensates, using high-resolution interferometric data.

The family of solutions derived here provides a robust theoretical foundation for exploring the strong-field phenomenology of KR gravity and its interplay with environmental anisotropy. A primary future direction is to extend these static metrics to stationary and rotating configurations, a necessary step for direct comparison with current and next-generation Event Horizon Telescope (ngEHT) data. For such rotating counterparts, the KR coupling ℓ and fluid parameter K are expected to induce measurable asymmetries in the shadow morphology and the displacement of the photon ring, potentially providing a unique signature of Lorentz symmetry breaking. Furthermore, the dynamical stability and gravitational-wave signatures of these spacetimes can be probed through their Quasinormal Mode (QNM) spectra. The modifications to the effective potential introduced by the KR field are likely to yield distinctive shifts in the damping rates and oscillation frequencies of the $\ell = 2$ fundamental mode, providing a pathway for verification by future space-based detectors such as LISA. Additionally, these solutions provide a framework for modelling quasi-periodic oscillations (QPOs) in the X-ray spectra of accreting black hole binaries.

Appendix A: Derivation of the Approximate Root Eq. (52) for Small K

We consider the equation

$$\left[1-\ell+K(\ell-\tfrac{1}{2})r^{1/(1-\ell)}\right]r-3(1-\ell)^2M=0, \tag{A1}$$

with $-1<\ell<1$ and K treated as a small parameter. Let

$$A=1-\ell>0, \qquad B=\ell-\tfrac{1}{2}, \qquad C=\frac{KB}{A}, \qquad D=3AM.$$

The equation becomes

$$r+C\,r^{1+\frac{1}{A}}-D=0, \tag{A2}$$

where we note

$$1+\frac{1}{A}=\frac{2-\ell}{1-\ell}\equiv n.$$

For $-1<\ell<1$, we have $n>0$. We expand the root $r(K)$ as

$$r(K)=r_0+r_1K+r_2K^2+\mathcal{O}(K^3). \tag{A3}$$

Substituting into (A2) gives

$$r_0+r_1K+r_2K^2+\cdots+\frac{B}{A}K\big(r_0+r_1K+\cdots\big)^n-D=0. \tag{A4}$$

Setting $K=0$ in (A4) yields

$$r_0-D=0 \quad\Longrightarrow\quad r_0=D=3(1-\ell)M. \tag{A5}$$

Expand $(r_0+r_1K+\cdots)^n=r_0^n+nr_0^{n-1}r_1K+\mathcal{O}(K^2)$. The $\mathcal{O}(K)$ part of (A3) is

$$r_1K+\frac{B}{A}Kr_0^n=0,$$

so

$$r_1=-\frac{B}{A}\,r_0^n. \tag{A6}$$

Since $B = \ell - \frac{1}{2}$, $A = 1 - \ell$, and $r_0 = 3(1-\ell)M$,

$$r_0^n = \left[3(1-\ell)M\right]^{\frac{2-\ell}{1-\ell}}.$$

Hence

$$r_1 = -\frac{\ell - \frac{1}{2}}{1-\ell}\left[3(1-\ell)M\right]^{\frac{2-\ell}{1-\ell}} \tag{A7}$$

$$r(K) \approx 3(1-\ell)M \; - \; \frac{\ell - \frac{1}{2}}{1-\ell}\left[3(1-\ell)M\right]^{\frac{2-\ell}{1-\ell}} K \; + \; \mathcal{O}(K^2) \tag{A8}$$

For the Special case $\ell = 1/2$, we have $B = 0$, so $r_1 = 0$ and the term proportional to K vanishes identically. Equation (A2) reduces to $r - D = 0$, giving the exact solution

$$r = 3(1 - \tfrac{1}{2})M = \frac{3M}{2},$$

independent of K, in agreement with (A8).

ACKNOWLEDGMENTS

The work of M.F. has been supported by Universidad Central de Chile through the project No. PDUCEN20240008.

[1] V. A. Kostelecky and S. Samuel, "Spontaneous Breaking of Lorentz Symmetry in String Theory," *Phys. Rev. D*, vol. 39, p. 683, 1989.

[2] T. Jacobson and D. Mattingly, "Gravity with a dynamical preferred frame," *Phys. Rev. D*, vol. 64, p. 024028, 2001.

[3] S. M. Carroll, J. A. Harvey, V. A. Kostelecky, C. D. Lane, and T. Okamoto, "Noncommutative field theory and Lorentz violation," *Phys. Rev. Lett.*, vol. 87, p. 141601, 2001.

[4] J. Alfaro, H. A. Morales-Tecotl, and L. F. Urrutia, "Loop quantum gravity and light propagation," *Phys. Rev. D*, vol. 65, p. 103509, 2002.

[5] S. L. Dubovsky, P. G. Tinyakov, and I. I. Tkachev, "Massive graviton as a testable cold dark matter candidate," *Phys. Rev. Lett.*, vol. 94, p. 181102, 2005.

[6] A. G. Cohen and S. L. Glashow, "Very special relativity," *Phys. Rev. Lett.*, vol. 97, p. 021601, 2006.

[7] G. R. Bengochea and R. Ferraro, "Dark torsion as the cosmic speed-up," *Phys. Rev. D*, vol. 79, p. 124019, 2009.

[8] P. Horava, "Quantum Gravity at a Lifshitz Point," *Phys. Rev. D*, vol. 79, p. 084008, 2009.

[9] V. A. Kostelecky, "Gravity, Lorentz violation, and the standard model," *Phys. Rev. D*, vol. 69, p. 105009, 2004.

[10] R. Bluhm, N. L. Gagne, R. Potting, and A. Vrublevskis, "Constraints and Stability in Vector Theories with Spontaneous Lorentz Violation," *Phys. Rev. D*, vol. 77, p. 125007, 2008. [Erratum: Phys.Rev.D 79, 029902 (2009)].

[11] Q. G. Bailey and V. A. Kostelecky, "Signals for Lorentz violation in post-Newtonian gravity," *Phys. Rev. D*, vol. 74, p. 045001, 2006.

[12] V. A. Kostelecky and S. Samuel, "Phenomenological Gravitational Constraints on Strings and Higher Dimensional Theories," *Phys. Rev. Lett.*, vol. 63, p. 224, 1989.

[13] V. A. Kostelecky and S. Samuel, "Gravitational Phenomenology in Higher Dimensional Theories and Strings," *Phys. Rev. D*, vol. 40, pp. 1886–1903, 1989.

[14] R. Casana, A. Cavalcante, F. P. Poulis, and E. B. Santos, "Exact Schwarzschild-like solution in a bumblebee gravity model," *Phys. Rev. D*, vol. 97, no. 10, p. 104001, 2018.

[15] A. Övgün, K. Jusufi, and İ. Sakallı, "Exact traversable wormhole solution in bumblebee gravity," *Phys. Rev. D*, vol. 99, no. 2, p. 024042, 2019.

[16] İ. Güllü and A. Övgün, "Schwarzschild-like black hole with a topological defect in bumblebee gravity," *Annals Phys.*, vol. 436, p. 168721, 2022.

[17] A. Ovgün, K. Jusufi, and I. Sakalli, "Gravitational lensing under the effect of Weyl and bumblebee gravities: Applications of Gauss–Bonnet theorem," *Annals Phys.*, vol. 399, pp. 193–203, 2018.

[18] S. Kanzi and İ. Sakallı, "GUP Modified Hawking Radiation in Bumblebee Gravity," *Nucl. Phys. B*, vol. 946, p. 114703, 2019.

[19] K. M. Amarilo, M. B. F. Filho, A. A. A. Filho, and J. A. A. S. Reis, "Gravitational waves effects in a Lorentz–violating scenario," *Phys. Lett. B*, vol. 855, p. 138785, 2024.

[20] D. Liang, R. Xu, X. Lu, and L. Shao, "Polarizations of gravitational waves in the bumblebee gravity model," *Phys. Rev. D*, vol. 106, no. 12, p. 124019, 2022.

[21] C. Ding, X. Chen, and X. Fu, "Einstein-Gauss-Bonnet gravity coupled to bumblebee field in four dimensional spacetime," *Nucl. Phys. B*, vol. 975, p. 115688, 2022.

[22] R.-H. Lin, R. Jiang, and X.-H. Zhai, "Quasinormal modes of the spherical bumblebee black holes with a global monopole," *Eur. Phys. J. C*, vol. 83, no. 8, p. 720, 2023.

[23] X. Zhang, M. Wang, and J. Jing, "Quasinormal modes and late time tails of perturbation fields on a Schwarzschild-like black hole with a global monopole in the Einstein-bumblebee theory," *Sci. China Phys. Mech. Astron.*, vol. 66, no. 10, p. 100411, 2023.

[24] R. Xu, D. Liang, and L. Shao, "Bumblebee Black Holes in Light of Event Horizon Telescope Observations," *Astrophys. J.*, vol. 945, no. 2, p. 148, 2023.

[25] R. Xu, D. Liang, and L. Shao, "Static spherical vacuum solutions in the bumblebee gravity model," *Phys. Rev. D*, vol. 107, no. 2, p. 024011, 2023.

[26] R. V. Maluf and J. C. S. Neves, "Black holes with a cosmological constant in bumblebee gravity," *Phys. Rev. D*, vol. 103, no. 4, p. 044002, 2021.

[27] Y. Sekhmani, A. Baruah, S. K. Maurya, J. Rayimbaev, M. Altanji, I. Ibragimov, and S. Muminov, "Kalb-Ramond black holes sourced by ModMax electrodynamics: Some perturbative properties in the phantom sector," *Phys. Dark Univ.*, vol. 50, p. 102157, 2025.

[28] Y. Sekhmani, S. K. Maurya, J. Rayimbaev, M. Altanji, I. Ibragimov, and S. Muminov, "Lorentz-violating ModMax black holes in phantom-enhanced Kalb–Ramond gravity: Thermodynamics and topological charges," *Phys. Dark Univ.*, vol. 50, p. 102079, 2025.

[29] B. Shodikulov, M. Mirov, F. Atamurotov, S. G. Ghosh, and A. Abdujabbarov, "Impact of Kalb–Ramond fields and perfect fluid dark matter on black hole shadows and gravitational lensing," *Phys. Dark Univ.*, vol. 50, p. 102096, 2025.

[30] M. Afrin, S. G. Ghosh, and A. Wang, "Testing EGB gravity coupled to bumblebee field and black hole parameter estimation with EHT observations," *Phys. Dark Univ.*, vol. 46, p. 101642, 2024.

[31] Z. Cai and R.-J. Yang, "Accretion of the Vlasov gas onto a Schwarzschild-like black hole," *Phys. Dark Univ.*, vol. 42, p. 101292, 2023.

[32] R.-J. Yang, H. Gao, Y. Zheng, and Q. Wu, "Effects of Lorentz breaking on the accretion onto a Schwarzschild-like black hole," *Commun. Theor. Phys.*, vol. 71, no. 5, pp. 568–572, 2019.

[33] S. U. Islam, S. G. Ghosh, and S. D. Maharaj, "Investigating rotating black holes in bumblebee gravity: insights from EHT observations," *JCAP*, vol. 12, p. 047, 2024.

[34] B. Altschul, Q. G. Bailey, and V. A. Kostelecky, "Lorentz violation with an antisymmetric tensor," *Phys. Rev. D*, vol. 81, p. 065028, 2010.

[35] K. K. Nair and A. M. Thomas, "Kalb-Ramond field-induced cosmological bounce in generalized teleparallel gravity," *Phys. Rev. D*, vol. 105, no. 10, p. 103505, 2022.

[36] S. Chakraborty and S. SenGupta, "Strong gravitational lensing — A probe for extra dimensions and Kalb-Ramond field," *JCAP*, vol. 07, p. 045, 2017.

[37] M. Kalb and P. Ramond, "Classical direct interstring action," *Phys. Rev. D*, vol. 9, pp. 2273–2284, 1974.

[38] W. F. Kao, W. B. Dai, S.-Y. Wang, T.-K. Chyi, and S.-Y. Lin, "Induced Einstein-Kalb-Ramond theory and the black hole," *Phys. Rev. D*, vol. 53, pp. 2244–2247, 1996.

[39] L. A. Lessa, J. E. G. Silva, R. V. Maluf, and C. A. S. Almeida, "Modified black hole solution with a background Kalb–Ramond field," *Eur. Phys. J. C*, vol. 80, no. 4, p. 335, 2020.

[40] R. Kumar, S. G. Ghosh, and A. Wang, "Gravitational deflection of light and shadow cast by rotating Kalb-Ramond black holes," *Phys. Rev. D*, vol. 101, no. 10, p. 104001, 2020.

[41] R. V. Maluf and J. C. S. Neves, "Bianchi type I cosmology with a Kalb–Ramond background field," *Eur. Phys. J. C*, vol. 82, no. 2, p. 135, 2022.

[42] L. A. Lessa, R. Oliveira, J. E. G. Silva, and C. A. S. Almeida, "Traversable wormhole solution with a background Kalb–Ramond field," *Annals Phys.*, vol. 433, p. 168604, 2021.

[43] K. Yang, Y.-Z. Chen, Z.-Q. Duan, and J.-Y. Zhao, "Static and spherically symmetric black holes in gravity with a background Kalb-Ramond field," *Phys. Rev. D*, vol. 108, no. 12, p. 124004, 2023.

[44] S. Tadaki and S. Takagi, "Phenomenological Theory of the Equilibrium State of the System with a Black Hole and Radiation," *Progress of Theoretical Physics*, vol. 73, pp. 288–291, Jan. 1985.

[45] H.-C. Kim and Y. Lee, "Spherically Symmetric Wormholes with anisotropic matter," *JCAP*, vol. 09, p. 001, 2019.

[46] H. Stephani, D. Kramer, M. A. H. MacCallum, C. Hoenselaers, and E. Herlt, *Exact solutions of Einstein's field equations*. Cambridge Monographs on Mathematical Physics, Cambridge: Cambridge Univ. Press, 2003.

[47] M. S. R. Delgaty and K. Lake, "Physical acceptability of isolated, static, spherically symmetric, perfect fluid solutions of Einstein's equations," *Comput. Phys. Commun.*, vol. 115, pp. 395–415, 1998.

[48] I. Semiz, "All 'static' spherically symmetric perfect fluid solutions of Einstein's equations with constant equation of state parameter and finite-polynomial 'mass function'," *Rev. Math. Phys.*, vol. 23, pp. 865–882, 2011.

[49] T. Katsuragawa, S. Nojiri, S. D. Odintsov, and M. Yamazaki, "Relativistic stars in de Rham-Gabadadze-Tolley massive gravity," *Phys. Rev. D*, vol. 93, p. 124013, 2016.

[50] S. H. Hendi, G. H. Bordbar, B. Eslam Panah, and S. Panahiyan, "Neutron stars structure in the context of massive gravity," *JCAP*, vol. 07, p. 004, 2017.

[51] S. H. Hendi, N. Riazi, and S. Panahiyan, "Holographical aspects of dyonic black holes: Massive gravity generalization," *Annalen Phys.*, vol. 530, no. 2, p. 1700211, 2018.

[52] A. A. Isayev, "Relativistic anisotropic stars with the polytropic equation of state in general relativity," *J. Phys. Conf. Ser.*, vol. 934, no. 1, p. 012039, 2017.

[53] N. Pant, N. Pradhan, and M. Malaver, "Anisotropic fluid star model in isotropic coordinates," 10 2014.

[54] T. Harko and M. K. Mak, "An Exact Anisotropic Quark Star Model," *Chin. J. Astron. Astrophys.*, vol. 2, no. 3, p. 248, 2002.

[55] M. K. Mak and T. Harko, "Anisotropic stars in general relativity," *Proc. Roy. Soc. Lond. A*, vol. 459, pp. 393–408, 2003.

[56] L. Herrera and N. O. Santos, "Local anisotropy in self-gravitating systems," *Phys. Rept.*, vol. 286, pp. 53–130, 1997.

[57] V. Varela, F. Rahaman, S. Ray, K. Chakraborty, and M. Kalam, "Charged anisotropic matter with linear or nonlinear equation of state," *Phys. Rev. D*, vol. 82, p. 044052, 2010.

[58] R. L. Bowers and E. P. T. Liang, "Anisotropic Spheres in General Relativity," *Astrophys. J.*, vol. 188, pp. 657–665, 1974.

[59] B. V. Ivanov, "Static charged perfect fluid spheres in general relativity," *Phys. Rev. D*, vol. 65, p. 104001, 2002.

[60] S. Carloni and D. Vernieri, "Covariant Tolman-Oppenheimer-Volkoff equations. II. The anisotropic case," *Phys. Rev. D*, vol. 97, no. 12, p. 124057, 2018.

[61] J. J. Matese and P. G. Whitman, "New method for extracting static equilibrium configurations in general relativity," *Physical Review D*, vol. 22, no. 6, p. 1270, 1980.

[62] C. G. Darwin, "The gravity field of a particle," *Proceedings of the Royal Society of London. Series A. Mathematical and Physical Sciences*, vol. 249, pp. 180 – 194, 1959.

[63] K. S. Virbhadra and G. F. R. Ellis, "Schwarzschild black hole lensing," *Phys. Rev. D*, vol. 62, p. 084003, 2000.

[64] V. Bozza, S. Capozziello, G. Iovane, and G. Scarpetta, "Strong field limit of black hole gravitational lensing," *Gen. Rel. Grav.*, vol. 33, pp. 1535–1548, 2001.

[65] V. Bozza, "Gravitational lensing in the strong field limit," *Phys. Rev. D*, vol. 66, p. 103001, 2002.

[66] F. Feleppa, V. Bozza, and O. Y. Tsupko, "Strong deflection limit analysis of black hole lensing in inhomogeneous plasma," *Phys. Rev. D*, vol. 110, no. 6, p. 064031, 2024.

[67] A. Bhadra, "Gravitational lensing by a charged black hole of string theory," *Phys. Rev. D*, vol. 67, p. 103009, 2003.

[68] R. Shaikh, P. Banerjee, S. Paul, and T. Sarkar, "Analytical approach to strong gravitational lensing from ultracompact objects," *Phys. Rev. D*, vol. 99, no. 10, p. 104040, 2019.

[69] R. Perna and C. R. Keeton, "Gravitational lensing of anisotropic sources," *Monthly Notices of the Royal Astronomical Society*, vol. 397, no. 2, pp. 1084–1092, 2009.

[70] E. L. B. Junior, J. T. S. S. Junior, F. S. N. Lobo, M. E. Rodrigues, D. Rubiera-Garcia, L. F. D. da Silva, and H. A. Vieira, "Gravitational lensing of a Schwarzschild-like black hole in Kalb-Ramond gravity," *Phys. Rev. D*, vol. 110, no. 2, p. 024077, 2024.

[71] K. Akiyama *et al.*, "First Sagittarius A* Event Horizon Telescope Results. VI. Testing the Black Hole Metric," *Astrophys. J. Lett.*, vol. 930, no. 2, p. L17, 2022.

[72] P. Kocherlakota *et al.*, "Constraints on black-hole charges with the 2017 EHT observations of M87*," *Phys. Rev. D*, vol. 103, no. 10, p. 104047, 2021.

[73] T. Do *et al.*, "Relativistic redshift of the star S0-2 orbiting the Galactic center supermassive black hole," *Science*, vol. 365, no. 6454, pp. 664–668, 2019.

[74] R. Abuter *et al.*, "Mass distribution in the Galactic Center based on interferometric astrometry of multiple stellar orbits," *Astron. Astrophys.*, vol. 657, p. L12, 2022.

[75] S. Kar, S. SenGupta, and S. Sur, "Static spherisymmetric solutions, gravitational lensing and perihelion precession in Einstein-Kalb-Ramond theory," *Phys. Rev. D*, vol. 67, p. 044005, 2003.

[76] C.-E. Fu, Y.-X. Liu, K. Yang, and S.-W. Wei, "q-Form fields on p-branes," *JHEP*, vol. 10, p. 060, 2012.

[77] S. Chakraborty and S. SenGupta, "Solutions on a brane in a bulk spacetime with Kalb-Ramond field," *Annals Phys.*, vol. 367, pp. 258–279, 2016.

[78] I. Cho and H.-C. Kim, "Simple black holes with anisotropic fluid," *Chin. Phys. C*, vol. 43, no. 2, p. 025101, 2019.

[79] S. Nojiri and S. D. Odintsov, "Unified cosmic history in modified gravity: from F(R) theory to Lorentz non-invariant models," *Phys. Rept.*, vol. 505, pp. 59–144, 2011.

[80] S. W. Hawking and G. F. R. Ellis, *The Large Scale Structure of Space-Time*. Cambridge Monographs on Mathematical Physics, Cambridge University Press, 2 2023.

[81] R. M. Wald, *General Relativity*. Chicago, USA: Chicago Univ. Pr., 1984.

[82] A. Einstein, "Die Feldgleichungen der Gravitation," *Sitzungsberichte der Königlich Preussischen Akademie der Wissenschaften*, pp. 844–847, Jan. 1915.

[83] S. Capozziello and M. De Laurentis, "Extended Theories of Gravity," *Phys. Rept.*, vol. 509, pp. 167–321, 2011.

[84] M. Afrin and S. G. Ghosh, "Testing Horndeski Gravity from EHT Observational Results for Rotating Black Holes," *Astrophys. J.*, vol. 932, no. 1, p. 51, 2022.

[85] R. Kumar and S. G. Ghosh, "Rotating black holes in $4d$ einstein-gauss-bonnet gravity and its shadow," *Journal of Cosmology and Astroparticle Physics*, vol. 2020, pp. 053–053, jul 2020.

[86] H. Ali, S. U. Islam, and S. G. Ghosh, "Shadows and parameter estimation of rotating quantum corrected black holes and constraints from EHT observation of M87* and Sgr A*," *JHEAp*, vol. 47, p. 100367, 2025.

[87] H. Ali and S. G. Ghosh, "Parameter estimation of Kerr-Bertotti-Robinson black holes using their shadows," *JCAP*, vol. 01, p. 018, 2026.

[88] A. Al-Badawi and F. Ahmed, "Spherically symmetric black hole with king dark matter halo," *The European Physical Journal C*, vol. 86, pp. 1434–6052, 2026.

[89] A. Al-Badawi and F. Ahmed, "A new black hole coupled with nonlinear electrodynamics surrounded by quintessence: Thermodynamics, geodesics, and regge–wheeler potential," *Chinese Journal of Physics*, vol. 94, pp. 185–203, 2025.

[90] A. Al-Badawi and M. Q. Owaidat, "Particle dynamics and shadow of a regular non-minimal magnetic black hole," *General Relativity and Gravitation*, vol. 55, 2023.

[91] F. Ahmed, A. Al-Badawi, and I. Sakalli, "Probing quantum gravity effects: Geodesic structure and thermodynamics of deformed schwarzschild ads black holes surrounded by cosmic strings," *Phys. Dark Univ.*, vol. 48, p. 101925, 2025.

[92] F. Ahmed, A. Al-Badawi, and İ. Sakallı, "Ads black strings in a cosmic web: geodesics, shadows, and thermodynamics," *Eur. Phys. J C*, vol. 85, no. 5, p. 554, 2025.

[93] V. Perlick and O. Y. Tsupko, "Calculating black hole shadows: Review of analytical studies," *Physics Reports*, vol. 947, pp. 1–39, 2022.

[94] K. Akiyama *et al.*, "First M87 Event Horizon Telescope Results. I. The Shadow of the Supermassive Black Hole," *Astrophys. J. Lett.*, vol. 875, p. L1, 2019.

[95] K. Akiyama *et al.*, "First M87 Event Horizon Telescope Results. VI. The Shadow and Mass of the Central Black Hole," *Astrophys. J. Lett.*, vol. 875, no. 1, p. L6, 2019.

[96] K. Akiyama *et al.*, "First M87 Event Horizon Telescope Results. III. Data Processing and Calibration," *Astrophys. J. Lett.*, vol. 875, no. 1, p. L3, 2019.

[97] K. Akiyama *et al.*, "First Sagittarius A* Event Horizon Telescope Results. I. The Shadow of the Supermassive Black Hole in the Center of the Milky Way," *Astrophys. J. Lett.*, vol. 930, no. 2, p. L12, 2022.

[98] K. Akiyama *et al.*, "First Sagittarius A* Event Horizon Telescope Results. I. The Shadow of the Supermassive Black Hole in the Center of the Milky Way," *Astrophys. J. Lett.*, vol. 930, no. 2, p. L12, 2022.

[99] [The Event Horizon Telescope Collaboration], P. Kocherlakota, *et al.*, "Constraints on black-hole charges with the 2017 EHT observations of M87*," *Physical Review D*, vol. 103, p. 104047, May 2021.

[100] S. Vagnozzi *et al.*, "Horizon-scale tests of gravity theories and fundamental physics from the Event Horizon Telescope image of Sagittarius A*," *Classical and Quantum Gravity*, vol. 40, p. 165007, Aug. 2023.

[101] C. Bambi, K. Freese, S. Vagnozzi, and L. Visinelli, "Testing the rotational nature of the supermassive object M87* from the circularity and size of its first image," *Phys. Rev. D*, vol. 100, no. 4, p. 044057, 2019.

[102] G. W. Gibbons and M. C. Werner, "Applications of the Gauss–Bonnet theorem to gravitational lensing," *Classical and Quantum Gravity*, vol. 25, p. 235009, Dec. 2008.

[103] M. C. Werner, "Gravitational lensing in the Kerr-Randers optical geometry," *General Relativity and Gravitation*, vol. 44, pp. 3047–3057, Dec. 2012.

[104] K. Jusufi, M. C. Werner, A. Banerjee, and A. Övgün, "Light deflection by a rotating global monopole spacetime," *Physical Review D*, vol. 95, p. 104012, May 2017.

[105] G. Crisnejo and E. Gallo, "Weak lensing in a plasma medium and gravitational deflection of massive particles using the Gauss-Bonnet theorem. A unified treatment," *Physical Review D*, vol. 97, p. 124016, June 2018.

[106] A. Övgün, K. Jusufi, and I. Sakallı, "Gravitational lensing under the effect of Weyl and bumblebee gravities: Applications of Gauss–Bonnet theorem," *Annals of Physics*, vol. 399, pp. 193–203, Dec. 2018.

[107] K. Jusufi and A. Övgün, "Effect of the cosmological constant on the deflection angle by a rotating cosmic string," *Physical Review D*, vol. 97, p. 064030, Mar. 2018.

[108] A. Övgün, "Weak field deflection angle by regular black holes with cosmic strings using the Gauss-Bonnet theorem," *Physical Review D*, vol. 99, p. 104075, May 2019.

[109] W. Javed, R. Babar, and A. Övgün, "Effect of the dilaton field and plasma medium on deflection angle by black holes in Einstein-Maxwell-dilaton-axion theory," *Physical Review D*, vol. 100, p. 104032, Nov. 2019.

[110] K. De Leon and I. Vega, "Weak gravitational deflection by two-power-law densities using the Gauss-Bonnet theorem," *Physical Review D*, vol. 99, p. 124007, June 2019.

[111] A. Övgün, I. Sakallı, and J. Saavedra, "Weak gravitational lensing by Kerr-MOG black hole and Gauss–Bonnet theorem," *Annals of Physics*, vol. 411, p. 167978, Dec. 2019.

[112] Z. Li and T. Zhou, "Equivalence of Gibbons-Werner method to geodesics method in the study of gravitational lensing," *Physical Review D*, vol. 101, p. 044043, Feb. 2020.

[113] W. Javed, A. Hamza, and A. Övgün, "Effect of nonlinear electrodynamics on the weak field deflection angle by a black hole," *Physical Review D*, vol. 101, p. 103521, May 2020.

[114] W. Javed, M. B. Khadim, J. Abbas, and A. Övgün, "Weak gravitational lensing by stringy black holes," *The European Physical Journal Plus*, vol. 135, p. 314, Mar. 2020.

[115] W. Javed, M. B. Khadim, J. Abbas, and A. Övgün, "Weak gravitational lensing by stringy black holes," *The European Physical Journal Plus*, vol. 135, p. 314, Mar. 2020.

[116] A. Ishihara, Y. Suzuki, T. Ono, T. Kitamura, and H. Asada, "Gravitational bending angle of light for finite distance and the gauss-bonnet theorem," *Phys. Rev. D*, vol. 94, p. 084015, Oct 2016.

[117] A. Ishihara, Y. Suzuki, T. Ono, and H. Asada, "Finite-distance corrections to the gravitational bending angle of light in the strong deflection limit," *Phys. Rev. D*, vol. 95, p. 044017, Feb 2017.

[118] K. S. Virbhadra, D. Narasimha, and S. M. Chitre, "Role of the scalar field in gravitational lensing," *Astron. Astrophys.*, vol. 337, pp. 1–8, 1998.

[119] S. U. Islam, J. Kumar, and S. G. Ghosh, "Strong gravitational lensing by rotating Simpson-Visser black holes," *JCAP*, vol. 10, p. 013, 2021.

[120] S. U. Islam and S. G. Ghosh, "Strong field gravitational lensing by hairy Kerr black holes," *Phys. Rev. D*, vol. 103, no. 12, p. 124052, 2021.

[121] A. Vachher, A. Kumar, and S. G. Ghosh, "The influence of uniform magnetic fields on strong field gravitational lensing by Kerr black holes," *JCAP*, vol. 11, p. 021, 2025.

[122] S. U. Islam, S. G. Ghosh, and S. D. Maharaj, "Strong gravitational lensing by Bardeen black holes in 4D EGB gravity: Constraints from supermassive black holes," *Chin. J. Phys.*, vol. 89, pp. 1710–1724, 2024.

[123] A. Vachher, S. U. Islam, R. Kumar Walia, and S. G. Ghosh, "Testing strong gravitational lensing effects of supermassive black holes with string-inspired metric: Observational signatures and EHT constraints," *Annals Phys.*, vol. 480, p. 170084, 2025.

[124] R. Kumar, S. U. Islam, and S. G. Ghosh, "Gravitational lensing by charged black hole in regularized $4D$ Einstein–Gauss–Bonnet gravity," *Eur. Phys. J. C*, vol. 80, no. 12, p. 1128, 2020.

[125] S. U. Islam, R. Kumar, and S. G. Ghosh, "Gravitational lensing by black holes in the $4D$ Einstein-Gauss-Bonnet gravity," *JCAP*, vol. 09, p. 030, 2020.

[126] V. Bozza, "A Comparison of approximate gravitational lens equations and a proposal for an improved new one," *Phys. Rev. D*, vol. 78, p. 103005, 2008.

[127] A. Kumar, S. U. Islam, and S. G. Ghosh, "Probing Lorentz Symmetry Violation through Lensing Observables of Rotating Black Holes," 8 2025.

[128] [The Event Horizon Telescope Collaboration], K. Akiyama, *et al.*, "First M87 Event Horizon Telescope Results. IV. Imaging the Central Supermassive Black Hole," *Astrophys. J. Lett.*, vol. 875, no. 1, p. L4, 2019.

[129] [The Event Horizon Telescope Collaboration], K. Akiyama, *et al.*, "First Sagittarius A* Event Horizon Telescope results. I. The shadow of the supermassive black hole in the center of the Milky Way.," *Astrophys. J. Lett.*, vol. 930, no. 2, p. L12, 2022.

[130] K. Akiyama *et al.*, "First M87 Event Horizon Telescope Results. V. Physical Origin of the Asymmetric Ring," *Astrophys. J. Lett.*, vol. 875, no. 1, p. L5, 2019.

[131] A. F. Zakharov, "Shadows around at Sgr A* and M87* as a tool to test gravity theories," in *ICRANet-ISFAHAN Astronomy Meeting: From the Ancient Persian Astronomy to Recent Developments in Theoretical and Experimental Physics, Astrophysics and General Relativity*, 8 2022.

[132] A. Vachher and S. G. Ghosh, "Strong gravitational lensing by rotating quantum-corrected black holes: Insights and constraints from EHT observations of M87* and Sgr A*," *JHEAp*, vol. 45, pp. 75–86, 2025.

[133] R. Kumar Walia, S. G. Ghosh, and S. D. Maharaj, "Testing Rotating Regular Metrics with EHT Results of Sgr A*," *Astrophys. J.*, vol. 939, no. 2, p. 77, 2022.

[134] S. G. Ghosh and M. Afrin, "An Upper Limit on the Charge of the Black Hole Sgr A* from EHT Observations," *Astrophys. J.*, vol. 944, no. 2, p. 174, 2023.

[135] J. Kumar, S. U. Islam, and S. G. Ghosh, "Strong gravitational lensing by loop quantum gravity motivated rotating black holes and EHT observations," *Eur. Phys. J. C*, vol. 83, no. 11, p. 1014, 2023.

[136] S. U. Islam, J. Kumar, R. Kumar Walia, and S. G. Ghosh, "Investigating Loop Quantum Gravity with Event Horizon Telescope Observations of the Effects of Rotating Black Holes," *Astrophys. J.*, vol. 943, no. 1, p. 22, 2023.

[137] I. Banerjee, S. Sau, and S. SenGupta, "Do shadows of Sgr A* and M87* indicate black holes with a magnetic monopole charge?," 7 2022.